Construction and Building Materials 531 (2026) 146522

Contents lists available at ScienceDirect

Construction and Building Materials

journal homepage: www.elsevier.com/locate/conbuildmat

Scale-bridging characterization and modeling of statistically inhomogeneous Moso bamboo

Lukas Speichinger [a], Ralf Förster [b], Thomas Böhlke [a,*]

[a] Institute of Engineering Mechanics, Chair for Continuum Mechanics, Karlsruhe Institute of Technology (KIT), Kaiserstraße 10, Karlsruhe, 76131, Germany
[b] Berliner Hochschule für Technik (BHT), Luxemburger Straße 10, Berlin, 13353, Germany

ARTICLE INFO

Keywords:
Moso bamboo
Statistically inhomogeneous microstructure
Microstructure characterization
Microstructure generation
Representative volume elements
FFT
Homogenization

ABSTRACT

This study presents a multiscale framework for investigating the radial distribution of mesostructural characteristics and the resulting macroscopic linear elastic behavior of the statistically inhomogeneous culm wall of moso bamboo. The proposed framework, comprising characterization, reconstruction, and homogenization, enables spatially resolved predictions of macroscopic mechanical properties based on mesostructural input. A set of micromechanical descriptors for statistically inhomogeneous particle structures is defined using indicator and parameter functions. These descriptors are applied to bamboo cross-sections through advanced image processing, allowing for the extraction of spatially resolved features and differentiation between vascular bundle types. A reconstruction algorithm generates local surrogate models that preserve the prescribed mesostructural characteristics using optimized tessellation and area fraction control. Resolution and representativity studies ensure the validity of the reconstructed models across radial positions. Finally, classical mean-field and FFT-based homogenization methods are applied to compute the radial distribution of effective linear elastic properties. The presented framework enhances the understanding of structure–property relationship in bamboo and establishes a foundation for future bio-inspired or bamboo-based material design.

1. Introduction

1.1. State of the art

Bamboo is considered the fastest-growing plant in the world and is distinguished by exceptional mechanical properties, making it suitable for a wide range of applications. Unlike wood, bamboo reaches maturity within three to six years and often exhibits comparable specific strength and stiffness [1]. Its rapid growth and high availability position bamboo as an effective carbon sink, contributing to global efforts to reduce CO_2 emissions [2]. Due to its social, economic, and ecological potential, bamboo is increasingly considered a sustainable alternative to conventional materials in industrial and infrastructural contexts [3]. Recent research explores its use in automotive structures [4], bamboo-reinforced concrete [5], and engineered timber products [6]. Moso bamboo, in particular, is widely used in industry and research due to its favorable structural characteristics [7]. To fully harness Moso bamboo's potential, a detailed understanding of its material behavior and underlying structural characteristics is essential.

The hierarchical anatomy of Moso bamboo and other species is documented by Liese [9]. Moso bamboo (*Phyllostachys pubescens/edulis*) belongs to a unique group of giant woody grasses (*Bambusoideae*) representing a part of the grass family (*Poaceae*). Unlike typical woody trees, bamboo is characterized by a primary growth, the culm, without significant secondary branching. For Moso bamboo, growth rates of up to 114.5 cm/day have been reported by Chen et al. [2]. As shown in Fig. 1, on the macroscopic level the culm consists of many segments called internodes. A longitudinal and transversal cut through an internode make expose its tubular structure and the partition walls at the connecting nodes. The internode cross-section reveals the mesostructure of the solid culm wall, which is a natural fiber-reinforced composite material. Dark, flower-shaped features correspond to vascular bundles that run parallel to the growth direction and interconnect at the nodes. Each bundle consists of conducting vessels encased by sclerenchymatous fiber sheaths and is embedded in a parenchymatous, foam-like matrix. According to investigations of Parameswaran and Liese [10], the lower scales reveal bamboo's cell structure and lamella composition of the cell wall, aspects that are beyond the scope of this study but have been addressed in other research [11–13].

First quantitative characterization of the internodal mesostructure by Nogata and Takahashi [14] and Amada et al. [15] show that the vascular bundles exhibit a spatially varying arrangement and morphology in radial direction. In their studies, the culm wall specimens

* Corresponding author.
E-mail address: thomas.boehlke@kit.edu (T. Böhlke).

https://doi.org/10.1016/j.conbuildmat.2026.146522
Received 11 December 2025; Received in revised form 10 April 2026; Accepted 27 April 2026
Available online 15 May 2026

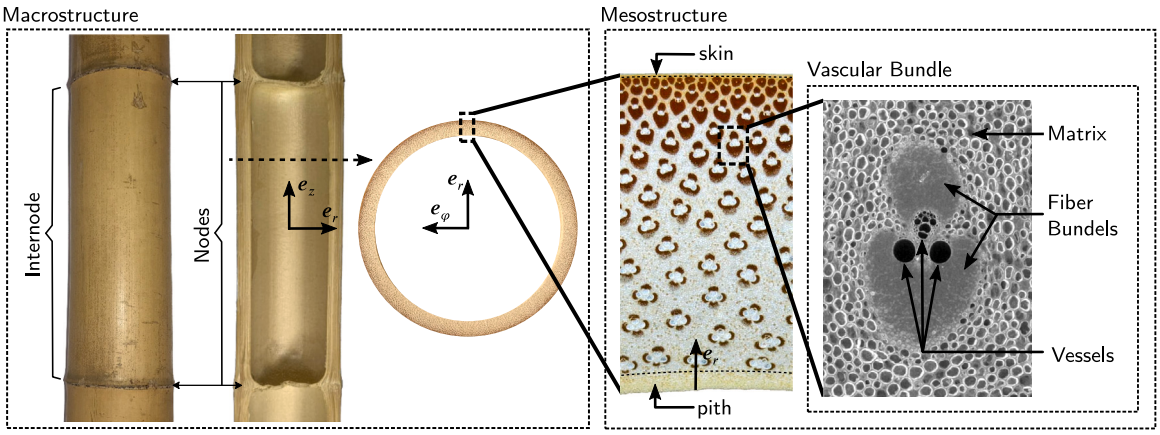

Fig. 1. The hierarchical anatomy of the bamboo culm on macroscopic and mesoscopic scale. The culm consists of multiple tubular internodes connected by nodes. The culm wall can be described as a composite material composed of vascular bundles embedded in a parenchymatous matrix, where the vascular bundle consists of the plants conducting vessels and sclerenchymatous fiber bundles [8].

are divided radially into multiple slices with consequently different structural and mechanical properties. Fiber bundle volume fraction and the linear elastic behavior in longitudinal direction are measured via image analysis and tensile tests correspondingly. Matrix and the fiber bundle properties are extrapolated from the experimental data using a linear rule of mixture, a procedure subsequently refined in later studies. Shao et al. [16] and Li and Shen [17] compare tensile tests with bamboo slices and single vascular bundle specimens. Liu et al. [18] and Shang et al. [19] use updated imaging techniques and image analysis software to investigate single vascular bundles in more detail. Using scanning electron microscopy to resolve the hollow conducting vessels and the cellular structure of fiber bundles and matrix material, Dixon and Gibson [8] and Osorio et al. [20] advance the characterization of mesoscopic properties by incorporating more detailed structural information. Li et al. [21] investigated the volumetric averages of fiber bundle volume fraction and distribution density of vascular bundles, which were automatically detected using a machine learning model based on the you-only-look-once (YOLO) algorithm introduced by Redmon et al. [22]. Building on this approach, Xu et al. [23,24] apply the detection model to characterize individual vascular bundles in terms of their cross-sectional fiber bundle area and aspect ratio. Furthermore, Tsuyama et al. [25] train a generative model on image data of individual vascular bundles to predict bundle morphology at different radial positions. Following Quintanilla and Torquato [26], the bamboo mesostructure is a statistically inhomogeneous particle structure. A statistical description of such a composite is provided by Torquato [27], which establishes a generalized mathematical setting to characterize heterogeneous random media.

Modeling an entire bamboo culm as hierarchical composite material with a monolithic approach that resolves structural features across all scales would be impractical in terms of computational resources. Instead, based on the characterized structural and mechanical properties at the mesoscopic scale, scale-bridging methods are employed to establish an effective medium description that captures the macroscopic response of the internodal culm wall. This strategy, commonly denoted by homogenization, is generally divided into different approaches, e.g. asymptotic homogenization, stochastic homogenization, local, first-order homogenization and non-local, higher-order homogenization.

Asymptotic homogenization replaces a material with finely periodic oscillating properties by an equivalent homogeneous continuum by a two-scale expansion and a limit process as the characteristic microstructural length tends to zero, yielding constant effective tensors from a linear periodic cell problem. For statistically inhomogeneous microstructure with sufficiently small gradients, the material coefficients depend not only on the fast periodic variable but also slowly on the macroscopic position. A scale separation must still hold, so that the material can be treated as locally periodic and the limit as the characteristic microstructural length tends to zero remains well defined [28].

Stochastic homogenization with locally stationary random fields replaces periodicity by local statistical stationarity while still requiring scale separation and sufficiently small or slowly varying gradients of the microstructural statistics. As a result, the effective constitutive law remains local and can be position-dependent [29,30]. Besides, scale-dependent, stochastic homogenization enables the investigation of auto- and cross-correlations of spatially varying material properties, modeled as random tensorial fields [31]. Accordingly, Savvas et al. [32] employs a moving-window technique to capture local variations of the volume fraction and corresponding apparent properties.

First-order homogenization methods determine the macroscopic constitutive response from a locally defined microstructural problem while assuming scale separation. The microstructural problem can be solved by mean-field or full-field approaches. The mean-field method derives analytical expressions for the macroscopic behavior by a simplified description of the microstructure, e.g., by simple inclusion geometries [33,34]. The approach incorporates the dominating correlation function, such as the volume fraction as one-point correlation function, and generally describes not only the mean values of stress and strain in the phases but also higher-order moments. In contrast, full-field techniques solve the boundary-value problem on a given statistically representative volume element (RVE) of the microstructure predominantly by numerical means, where the governing equations are resolved either with conventional physics-based solvers [35] or with data-driven algorithms [36]. Representative applications are provided by Chao et al. [37] demonstrating mean-field homogenization with microstructure descriptors including fractal geometry of porous media, and by Ma and Truster [38] investigating hypoelastic plasticity at finite strains by applying an advanced homogenization technique based on the Fast Fourier Transformation (FFT), as comprehensively studied by Schneider [39]. Kuhn et al. [40], Su et al. [41] and Lauff et al. [42,43] develop optimization algorithms to generate RVEs with prescribed characteristics of polycrystals, porous media and fiber-reinforced composites, respectively. Gajek et al. [44] addresses spatially varying characteristics by employing deep material networks (DMN) as local surrogates.

Non-local homogenization derives higher-order continuum models in which gradients of macroscopic fields explicitly appear in the constitutive relations [45]. This approach becomes necessary when classical scale separation is no longer clearly satisfied or when the microstructure gradients are not sufficiently small [46].

Considering the bamboo mesostructure, other studies have employed first-order homogenization to characterize the macroscopic behavior of the bamboo material. Palombini et al. [47] investigates the axial compressive strength of the bamboo culm wall using Finite Element Analysis (FEA) of a morphological model reconstructed from μCT data. To consider the anisotropy of the culm wall stiffness, Cui et al. [48] propose a numerical homogenization approach using FEA with a simplified morphological model of a single vascular bundle. Al-Rukaibawi et al. [49] advances this approach by introducing a anatomy-based model of a vascular bundle and compares the numerical results with mean-field homogenization models at four given radial positions. To the best of the authors knowledge, this represents the state-of-the-art modeling approach for the bamboo mesostructure, as applied in recent studies such as Khajouei-Nezhad et al. [50].

1.2. Objectives

Despite significant progress in the experimental characterization and numerical modeling of bamboo's mesostructure, current approaches often fall short of leveraging advanced micromechanical and numerical methods that are well-established in the broader field of composite materials. Existing studies primarily focus on mean material properties and simplified structural models, often probing only a limited number of radial positions within the culm wall. As a result, they fail to fully capture and exploit the radial distribution of structural and mechanical properties. To overcome these limitations, this study integrates modern multiscale methods into the analysis of bamboo's mesostructure, pursuing the following specific objectives

- Realizing a more accurate and spatially resolved analysis of the culm wall's macroscopic mechanical response based on mesostructural data.
- Definition of micromechanical descriptors and characteristics for statistically inhomogeneous particle structures, based on the formulations presented by Torquato [27].
- Application of this generalized characterization framework to the bamboo mesostructure using advanced image processing techniques, enabling the extraction of spatially resolved structural features from internode cross-sections.
- Development of anatomy-based surrogate models of the mesostructure by reconstructing volume elements that reflect the local characteristics and are representative regarding their macroscopic mechanical behavior.
- Application of classical mean-field and numerical FFT-based homogenization methods for computing the radial distribution of the effective linear elastic properties of the bamboo culm wall.

The manuscript is organized as follows. In Section 2 the methods and material used are described, including the general characterization of statistically inhomogeneous particle structures (Section 2.1), the computational characterization of the bamboo mesostructure (Section 2.2), the reconstruction of local surrogate models of the mesostructure (Section 2.3) and the micromechanical homogenization methods (Section 2.4). The result of the applied methods are discussed in Section 3. Particularly, the measured characteristics of the bamboo mesostructure (Section 3.1), the generated representative images (Section 3.2) and the predictions of the homogenization models (Section 3.3) are presented and compared to literature results. The findings are concluded in Section 4, and additional material is given in Appendices A–F.

1.3. Notation

In this manuscript, a direct tensor notation is employed. Scalars are denoted by non-bold Greek or Latin letters, e.g. α, V. Tensors of first order or vectors are represented by lower-case, Greek or Latin bold letters, e.g. $\boldsymbol{\varphi}$, $\boldsymbol{b}$, whereas second-order tensors are given by upper-case Latin or lower-case Greek bold letters, e.g. $\boldsymbol{A}$, $\boldsymbol{\sigma}$ and fourth-order tensors by upper-case Latin blackboard bold letters, e.g. $\mathbb{A}$, $\mathbb{B}$. The identity tensors of second and fourth order are denoted by $\boldsymbol{I}$ and $\mathbb{I}$, respectively, accordingly $\mathbb{I}^{\mathrm{S}}$ is the symmetric identity tensor of fourth order. Symmetric second-order tensors in three-dimensional vectors space are given in its diagonalized form by $\boldsymbol{B}\hat{=}\mathrm{diag}(b_1, b_2, b_3)$. The linear mapping of a first-order tensor by a second order tensor is denoted by, for example, $\boldsymbol{a} = \boldsymbol{C}\boldsymbol{b}$, and the linear mapping of a second-order tensor by a fourth-order tensor by, for example, $\boldsymbol{A} = \mathbb{C}[\boldsymbol{B}]$. The Scalar product is only defined between tensors of identical order and is represented by, for example, $a = \boldsymbol{a} \cdot \boldsymbol{b}$, $b = \boldsymbol{A} \cdot \boldsymbol{B}$. The dyadic product for tensors of any order is represented by, for example, $\boldsymbol{C} = \boldsymbol{a} \otimes \boldsymbol{b}$, $\mathbb{C} = \boldsymbol{A} \otimes \boldsymbol{B}$, and besides, the box product between second order tensors is defined by $(\boldsymbol{A}\square\boldsymbol{C})[\boldsymbol{B}] = \boldsymbol{A}\boldsymbol{B}\boldsymbol{C}$. Multiple dyadic products of a tensor with itself are denoted by $\mathbb{A}^{\otimes n}$. Tuples or lists of mathematical objects are denoted by underlined, non-bold Latin letters, e.g. $\underline{a}$. For additional details, the reader is referred to, for example, Gurtin et al. [51] and Moakher [52].

2. Material and methods

2.1. Characterization of statistically inhomogeneous particle structures

Microstructural descriptors

The microstructure of random heterogeneous materials with embedded particles, e.g. fibers, and inhomogeneous characteristics is called a statistically inhomogeneous particle structure. In Fig. 2(a) multiple realizations ω of a exemplary statistically inhomogeneous particle structure are shown. The set of all realizations is called the ensemble Ω. The volume of a realization V_ω is partitioned into multiple disjoint subsets or phases indexed by α. According to Torquato [27], the indicator function of phase α in a realization ω, also referred to as phase indicator function, is given by

$$I^{\alpha}_{\omega}(\boldsymbol{x}) = \begin{cases} 1 & \text{, if } \boldsymbol{x} \text{ in } \alpha \\ 0 & \text{, else} \end{cases} \tag{1}$$

and describes the spatial distribution of a phase by indicating, whether a given position $\boldsymbol{x} \in V_\omega$ lies inside phase α or not. Considering particle embedded structures, each phase, which is not the continuous matrix, can be divided in multiple disjoint and non-adjacent subsets or non-overlapping particles indexed by P. The set of all particles of phase α, also referred to as α-particles, of a realization ω is denoted by $\mathcal{P}^{\alpha}_{\omega}$ and

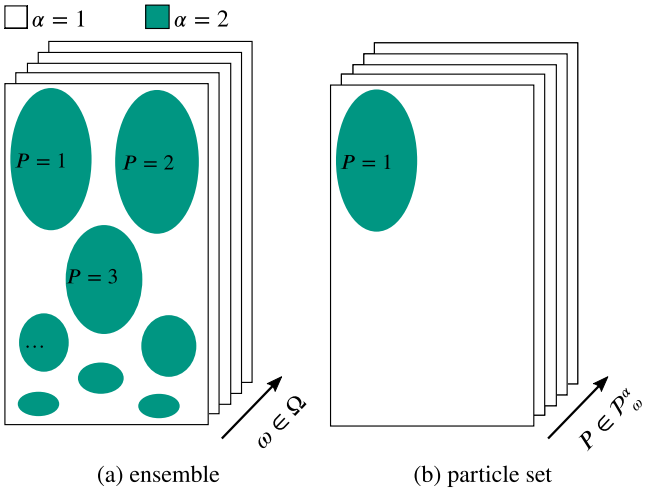

Fig. 2. Graphical representation of phase (a) and particle (b) indicator functions of a statistically inhomogeneous particle structure with two phases $\alpha = 1$ and 2, where phase 2 is divided in multiple non-overlapping particles.

depicted in Fig. 2(b). To describe the locality of a single particle, the indicator function of particle P of phase α in realization ω, also referred to as particle indicator function, is introduced by

$$I^{\alpha}_{\omega,P}(\boldsymbol{x}) = \begin{cases} 1 & \text{, if } \boldsymbol{x} \text{ in } P \text{ of } \alpha \\ 0 & \text{, else} \end{cases}, \tag{2}$$

which indicates, whether a given position x lies inside a specific particle P of phase α. Because the particles are non-overlapping, the phase indicator function of a realization is the sum of the related particle indicator functions, such that

$$I^{\alpha}_{\omega}(\boldsymbol{x}) = \sum_{P \in \mathcal{P}^{\alpha}_{\omega}} I^{\alpha}_{\omega,P}(\boldsymbol{x}). \tag{3}$$

The phase and particle indicator functions contain all information about the particle structure in binary form but can be condensed using a parameterized description of the particles. For a given realization ω and phase α, each particle P possesses a distinct morphology characterized by a set of morphological parameters

$$\underline{z}^{\alpha}_{\omega,P} = \left\{ V^{\alpha}_{\omega,P},\ \boldsymbol{Q}^{\alpha}_{\omega,P},\ s^{\alpha}_{\omega,P},\ \dots \right\}, \tag{4}$$

where $V^{\alpha}_{\omega,P}$ denotes the particle volume, $\boldsymbol{Q}^{\alpha}_{\omega,P} \in SO(3)$ represents the particle orientation as a proper orthogonal second-order tensor, and $s^{\alpha}_{\omega,P}$ specifies the particle shape. The ellipsis indicates the potential inclusion of additional morphological descriptors. The particle volume and orientation can be derived from the volume moments of the particle as given in Appendix C. The particle shape can be any kind of shape descriptor, for example the area and average curvature of the particle surface as proposed by Ohser and Mücklich [53]. The morphological parameters are assumed to be extensive measures and are uniformly assigned to every point that lies inside the according particle. This can be expressed by the so called parameter function of particle P of phase α in realization ω given by

$$\underline{Z}^{\alpha}_{\omega,P}(\boldsymbol{x}) = \begin{Bmatrix} \underline{z}^{\alpha}_{\omega,P} & \text{, if } \boldsymbol{x} \text{ in } P \text{ of } \alpha \\ \underline{0} & \text{, else} \end{Bmatrix} = \underline{z}^{\alpha}_{\omega,P} I^{\alpha}_{\omega,P}(\boldsymbol{x}), \tag{5}$$

which is the product of the particle indicator function and the corresponding morphological parameters and also referred to as specific parameter function. Here, $\underline{0}$ denotes the zero element of varying tensor order corresponding to the morphological parameters, e.g. $\underline{0} = \{0, \boldsymbol{0}, 0, \dots\}$ assuming the shape descriptor to be a scalar. The sum of the specific parameter functions over all particles in set $\mathcal{P}^{\alpha}_{\omega}$ leads to the parameter function of phase α in realization ω, also referred to as generic parameter function, given by

$$\underline{Z}^{\alpha}_{\omega}(\boldsymbol{x}) = \sum_{P \in \mathcal{P}^{\alpha}_{\omega}} Z^{\alpha}_{\omega,P}(\boldsymbol{x}). \tag{6}$$

If a given position $\boldsymbol{x}$ lies in a given particle, the generic parameter function returns the morphological parameters of this particle, otherwise it returns $\underline{0}$. Accordingly, the generic parameter function describes how the morphological parameters of α-particles are distributed inside a realization ω.

Microstructural characteristics of first and second order

With the indicator and parameter functions, describing the phase and particle morphology distributions, characteristics of the particle structure can be derived by statistical analysis. The characteristics are an estimate of how the structure would look like at a given position $\boldsymbol{x}$. For the statistical analysis the ensemble average is used, which is defined as the average over all realizations ω of the ensemble Ω and is given by

$$\langle \cdot \rangle = \lim_{|\Omega| \to \infty} \frac{1}{|\Omega|} \sum_{\omega \in \Omega} (\cdot)_{\omega} \approx \frac{1}{|\Omega|} \sum_{\omega \in \Omega} (\cdot)_{\omega}, \tag{7}$$

where $|\Omega|$ is the number of realizations of the ensemble. Assuming $|\Omega|$ is large enough to be statistically representative, the volume average can be applied to a finite set of realizations. By taking the ensemble average of the indicator function, the so called one-point probability function is derived as

$$S^{\alpha}_{1}(\boldsymbol{x}) = \left\langle I^{\alpha}_{\omega}(\boldsymbol{x}) \right\rangle =: v^{\alpha}(\boldsymbol{x}). \tag{8}$$

This first order characteristic is the probability to find phase α at a given position $\boldsymbol{x}$ and can be interpreted as the volume fraction of phase α. According to Torquato [27] any microstructure is fully characterized by the n-point probability functions, but in fact interpretability of higher order probability functions is lacking. Hence, interpretable characteristics describing the particle morphology are used. For this purpose, a subset of the ensemble Ω is introduced by

$$\Omega^{\alpha}(\boldsymbol{x}) = \{\omega | \omega \in \Omega, I^{\alpha}_{\omega}(\boldsymbol{x}) = 1\}, \tag{9}$$

which only includes the realizations having a particle of phase α at $\boldsymbol{x}$. Consequently, for the realization number of the sub ensemble holds

$$|\Omega^{\alpha}(\boldsymbol{x})| = \sum_{\omega \in \Omega} I^{\alpha}_{\omega}(\boldsymbol{x}). \tag{10}$$

This gives rise to the introduction of the so called phase average $\langle \cdot \rangle_{\alpha}$, which is the average over the sub ensemble $\Omega^{\alpha}(\boldsymbol{x})$ and defined by

$$\langle \cdot \rangle_{\alpha} = \frac{1}{|\Omega^{\alpha}(\boldsymbol{x})|} \sum_{\omega \in \Omega^{\alpha}} (\cdot)_{\omega}. \tag{11}$$

By taking the phase average of the generic parameter function for each parameter separately, the first statistical moment corresponding to the average particle morphology is obtained as

$$\underline{\mu}^{\alpha}(\boldsymbol{x}) = \left\{ \bar{V}^{\alpha},\ \bar{\boldsymbol{Q}}^{\alpha},\ \bar{s}^{\alpha},\ \dots \right\} = \left\langle \underline{Z}^{\alpha}_{\omega}(\boldsymbol{x}) \right\rangle_{\alpha}, \tag{12}$$

representing the particle morphology of phase α most likely to occur at position $\boldsymbol{x}$, i.e. the average particle volume $\bar{V}^{\alpha}$, average particle orientation $\bar{\boldsymbol{Q}}^{\alpha}$ and average particle shape $\bar{s}^{\alpha}$. In addition to the mean, higher-order statistical moments provide further insight into the stochastic variability of particle morphology within the sub-ensemble $\Omega^{\alpha}_{P}(\boldsymbol{x})$. E.g. second-order characteristics are given by the covariances of each morphological parameter, defined as

$$\underline{k}^{\alpha}(\boldsymbol{x}) = \left\langle \underline{Z}^{\alpha}_{\omega}(\boldsymbol{x})^{\otimes 2} \right\rangle_{\alpha} - \underline{\mu}^{\alpha}(\boldsymbol{x})^{\otimes 2}, \tag{13}$$

where the dyadic product is applied element-wise and reduces to a scalar product for tensors of zeroth order. Notably, for the particle orientation the corresponding statistical moments are related to other well studied statistical descriptors, e.g. texture coefficients for polycrystals Böhlke et al. [54] and fiber orientation tensors for fiber-reinforced composites Advani and Tucker [55]. According to Quintanilla and Torquato [26] the particle number density $n^{\alpha}(\boldsymbol{x})$ is a first-order characteristic to describe the arrangement or spatial distribution of particles centers. This characteristic is the one-particle probability density function of an ordinary Poisson field and defines the number of α-particles N^{α}, which can be found in an arbitrary volume element V by

$$N^{\alpha} = \int_{V} n^{\alpha}(\boldsymbol{x}) \, \mathrm{d}V. \tag{14}$$

Considering an infinitesimal volume element $\mathrm{d}V$ in the proximity of position $\boldsymbol{x}$ with a corresponding number of α-particles $\mathrm{d}N^{\alpha}$ a relation between the density, volume fraction and average particle volume is derived. For the mentioned characteristics inside $\mathrm{d}V$ holds

$$n^{\alpha}(\boldsymbol{x}) = \frac{\mathrm{d}N^{\alpha}}{\mathrm{d}V} = \frac{\mathrm{d}N^{\alpha} v^{\alpha}(\boldsymbol{x})}{\mathrm{d}V v^{\alpha}(\boldsymbol{x})} = \frac{\mathrm{d}N^{\alpha} v^{\alpha}(\boldsymbol{x})}{\mathrm{d}V^{\alpha}} = \frac{v^{\alpha}(\boldsymbol{x})}{\bar{V}^{\alpha}(\boldsymbol{x})}, \tag{15}$$

where the total Volume of α-particles is given by $\mathrm{d}V^{\alpha} = v^{\alpha}(\boldsymbol{x}) \mathrm{d}V = \bar{V}^{\alpha}(\boldsymbol{x}) \mathrm{d}N^{\alpha}$. Due to the derived relation, the particle number density is not an independent characteristic.

Type-specific characteristics

Assuming that the particles of a phase α can be divided into N^{α}_{T} types due to different morphologies, the statistical distribution of the morphological parameters is generally multi modal. As a consequence the average and standard deviation of parameters for all particles are

not sufficient to characterize the particle structure. In this case the particle set of a realization is split according to the different types obtaining type-specific particle subsets $\mathcal{P}_\omega^{\alpha,i}$ with $i = 1, \dots, N_\mathrm{T}^\alpha$. If the type is known for every particle and the stochastic distribution of the type-specific morphology parameters is normal, type-specific characteristics $v^{\alpha,i}$, $\underline{\mu}^{\alpha,i}$ and $\underline{k}^{\alpha,i}$ can be derived with Eqs. (8), (12) and (13). The required type-specific phase and parameter functions $I_\omega^{\alpha,i}$ and $\underline{Z}_\omega^{\alpha,i}$ are based on Eqs. (3) and (6) while summing over the type-specific particle subsets. To derive the overall volume fraction and number density of phase α, the type-specific characteristics are assembled using

$$v^\alpha(\boldsymbol{x}) = \sum_i v^{\alpha,i}(\boldsymbol{x}), \quad n^\alpha(\boldsymbol{x}) = \sum_i n^{\alpha,i}(\boldsymbol{x}). \tag{16}$$

The type fraction is defined as the ratio of type-specific and overall volume fraction denoted by $\phi^{\alpha,i} = v^{\alpha,i}/v^\alpha$. Considering Eq. (15), relation between number density, volume fraction and average particle volume only holds for the type-specific characteristics but not for the overall density n^α regarding the overall characteristics.

Volume averages and ergodic microstructure

In the general case of statistically inhomogeneous particle structures, the defined characteristics depend on the position $\boldsymbol{x}$. However, the volume-average d characteristics inside a volume V can be calculated by the integrated volume average of the corresponding spatial distributions given by

$$\begin{aligned} v_\mathrm{v}^\alpha &= \frac{1}{V}\int_V v^\alpha(\boldsymbol{x})\,\mathrm{d}V, \quad n_\mathrm{v}^\alpha = \frac{1}{V}\int_V n^\alpha(\boldsymbol{x})\,\mathrm{d}V, \\ \underline{\mu}_\mathrm{v}^\alpha &= \frac{1}{V^\alpha}\int_{V^\alpha} \underline{\mu}^\alpha(\boldsymbol{x})\,\mathrm{d}V, \quad \underline{k}_\mathrm{v}^\alpha = \frac{1}{V^\alpha}\int_{V^\alpha} \underline{k}^\alpha(\boldsymbol{x})\,\mathrm{d}V, \end{aligned} \tag{17}$$

where V^α is the total volume of phase α in V. If all characteristics are independent of $\boldsymbol{x}$, the particle structure can be called statistically homogeneous. A special case of statistical homogeneity is ergodicity. For ergodic structures the ensemble average is equal to the volume average of a single realization ω_0 with respect to the limit of an infinite ensemble and volume and it holds

$$\lim_{N\to\infty} \frac{1}{N}\sum_{\omega\in\Omega}(\cdot)_\omega = \lim_{V\to\infty}\frac{1}{V}\int_V (\cdot)_{\omega_0}\,\mathrm{d}V. \tag{18}$$

The same holds for the phase average because it considers a subset of the ensemble. It is to notice, that a ergodic particle structure could have different particle types embedded and the described type-specific characterization is still useful to deal with appearing multi modal distributions of the morphological parameters.

Table 1
Geometry of the investigated internodes.

IN	1	2	3	4	avg
L_IN in mm	267	269	272	277	271.25
D_IN in mm	87.22	84.19	82.44	80.85	83.68
δ_IN in mm	7.28	7.15	6.82	6.64	6.97

2.2. Mesostructure characterization based on image data

Material and imaging

The material investigated in this study consists of four-year-old Moso bamboo (*Phyllostachys pubescens*), provided by the supplier *CONBAM*. Four consecutive internodes were extracted from the central region of a bamboo culm, excluding the nodal sections. The geometric parameters of the internodes, namely length L_IN, outer diameter D_IN, and wall thickness δ_IN, are summarized in Table 1. From each internode, small ring-shaped sections were prepared. One surface corresponding to the transverse cross-section was polished using progressively finer abrasive papers, culminating in a grit size of P2000. The polished cross-sections were subsequently imaged with a digital microscope equipped with a 5 MP sensor. Given that the fiber bundles and tubular vessels exhibit negligible variation along the longitudinal axis, two-dimensional imaging is considered sufficient for representing the mesostructure. From the acquired images, radially oriented stripes were extracted. The upper and lower bounds of each stripe correspond to the outer and inner surfaces of the culm wall. Since the stripe width is significantly smaller than the internode diameter, the vertical and horizontal axes of the images can be assumed to approximate the radial and circumferential directions, respectively. For each internode, 10 to 15 cross-sectional stripes were generated, representing distinct realizations of the mesostructure. An exemplary realization is shown in Fig. 3(a). Due to the polishing process, the hollow capillary system becomes filled with abrasive dust, rendering the fiber bundles as the only discernible structural feature. Consequently, the present work focuses on the characterization of the fiber bundle phase, while the capillary system is treated as part of the matrix material. To investigate the capillary network in detail, alternative imaging techniques such as μCT scanning would be required. Nevertheless, the characterization methodology proposed herein is applicable to both the fiber bundle phase and the vessel phase.

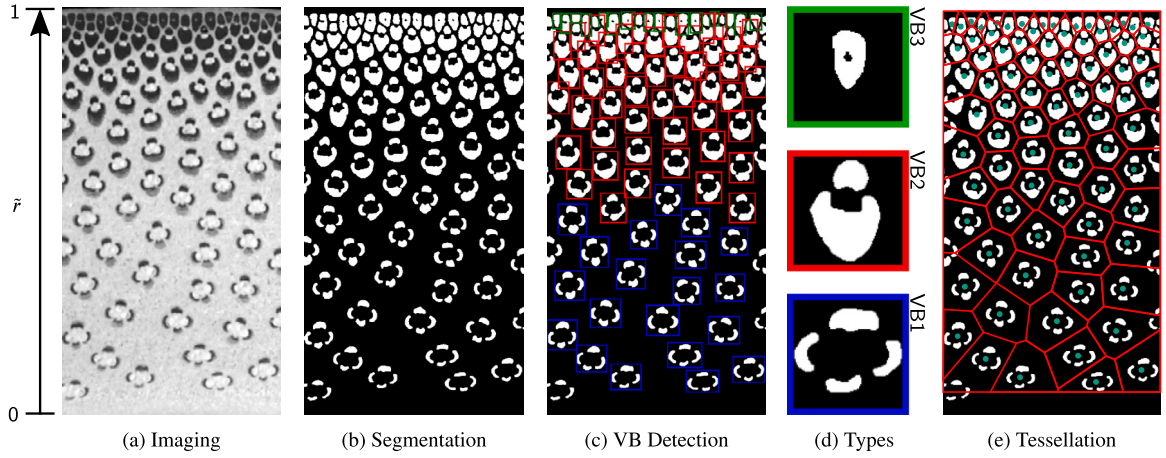

Fig. 3. Image processing steps of the mesostructure characterization including Imaging (a) of raw data, Segmentation (b) of fiber bundles and matrix and Detection (c) of Vascular Bundles. The vascular bundle types (d) VB1, VB2 and VB3 are marked by the colors blue, red and green, respectively. A Tessellation (e) is computed based on the morphological centers of the vascular bundles highlighted in green.

Segmentation and vascular bundle detection

To distinguish between the fiber bundle phase and the matrix material, image segmentation is applied to the cross sectional stripes. Therefore the Trainable Weka Segmentation tool of the image processing software FIJI is used [56,57]. An exemplary segmented stripe is shown in Fig. 3(b), where the white particles and the black background represent the fiber bundles and the matrix material, respectively. The segmented stripes are the discrete phase indicator functions of the fiber bundles and are called the indicator images denoted by

$$I^{\mathrm{fb}}_{\omega}[m,n] = I^{\mathrm{fb}}_{\omega}(m\boldsymbol{\Delta x} + n\boldsymbol{\Delta y}) \tag{19}$$

with $\boldsymbol{\Delta x}$ and $\boldsymbol{\Delta y}$ being the pixel vectors in horizontal and vertical direction, respectively. Pixel indices are denoted by $m = 1,\dots,N_{x,\omega}$ and $n = 1,\dots,N_{y,\omega}$, where $N_{x,\omega}$ and $N_{y,\omega}$ are the vertical and horizontal pixel count of realization ω, respectively. The image resolution is given by the pixel edge length $h = ||\boldsymbol{\Delta x}|| = ||\boldsymbol{\Delta y}||$. In case of the bamboo mesostructure the particles to investigate are not the individual fiber bundles but the vascular bundles (VB) consisting of multiple fiber bundles. According to Li et al. [21] the vascular bundles can divided into three different types regarding their fiber bundle number. Fig. 3(d) shows exemplary vascular bundles of type VB1, VB2 and VB3, which consist of four fiber bundles, two to three fiber bundles and a single fiber bundle, respectively. Investigations of Xu et al. [23] show that the you-only-look-once algorithm (YOLO), based on a convolutional neural network and introduced by Redmon et al. [22], delivers a fast and precise detection of vascular bundles. As visualized in Fig. 3(c), the YOLO-based detector predicts the bounding boxes and the type of vascular bundles. In this work, the Weka segmentation model and a YOLO implementation of Jocher et al. [58] is embedded in a python program for automated processing of the image stripes. More on the training and evaluation of the employed machine-learning models is documented in Appendix B.

Morphology measuring

Based on predictions of the trained detection model, images of individual vascular bundles are extracted as shown in Fig. 3(d). It occurs that the model detects truncated vascular bundles at the horizontal image bounds. These detections are ignored because they do not represent the complete vascular bundle morphology. The remaining extracted images work as the discrete particle indicator functions of the fiber bundle phase denoted by $I^{\mathrm{fb}}_{\omega,\mathrm{VB}}[m,n]$. Even though they only represent a section of the realizations space, the morphological parameters of a vascular bundle can be calculated according to Appendix C. Because of the reduced dimensionality, the morphological parameters are the cross-sectional fiber bundle area of a vascular bundle $A^{\mathrm{fb}}_{\omega,\mathrm{VB}}$, the vascular bundle orientation angle $\varphi^{\mathrm{fb}}_{\omega,\mathrm{VB}}$ with respect to the radial axis and the cross sectional shape $s^{\mathrm{fb}}_{\omega,\mathrm{VB}}$. The cross-sectional area is calculated using the discrete form of Eqs. (36) given by

$$A^{\mathrm{fb}}_{\omega,\mathrm{VB}} = \sum_m \sum_n I^{\mathrm{fb}}_{\omega,\mathrm{VB}}[m,n]h^2 \tag{20}$$

for all vascular bundles. The cross-sectional orientation is defined as the rotation of the principal system of the second-order area moment $\boldsymbol{J}^{\mathrm{fb}}_{\omega,\mathrm{VB}}$ given by Eq. (41). Because the rotation axis is aligned to the longitudinal direction $\boldsymbol{e}_z$ for all vascular bundles, only the rotation angle is statistically relevant, which is computed as

$$\tan(2\varphi^{\mathrm{fb}}_{\omega,\mathrm{VB}}) = \frac{2J^{\mathrm{fb}}_{\omega,\mathrm{VB},xy}}{J^{\mathrm{fb}}_{\omega,\mathrm{VB},xx} - J^{\mathrm{fb}}_{\omega,\mathrm{VB},yy}} \tag{21}$$

according to Eq. (42). For a isotropic inertia tensor, which is most likely the case for vascular bundles of type 1, the principal system is non-unique. In this case, the orientation of type 1 vascular bundles is defined as the orientation of the line connecting the centroids of the uppermost and lowermost fiber bundles, as illustrated in Fig. 4(a). Following Xu et al. [24] and Tsuyama et al. [25], the fiber bundle shape of a vascular bundle can be modeled using an elliptical representation enclosed within a rectangular bounding box. As depicted in Fig. 4(b), this box is aligned with the vascular bundle orientation and defines its spatial extent in the directions parallel and perpendicular to that orientation. Notably, the bounding box is not equal the predicted box of the detection model. The aspect ratio of the vascular bundle cross-section is denoted by $\alpha^{\mathrm{fb}}_{\omega,\mathrm{VB}} = h^{\mathrm{fb}}_{\omega,\mathrm{VB}}/w^{\mathrm{fb}}_{\omega,\mathrm{VB}}$, where $h^{\mathrm{fb}}_{\omega,\mathrm{VB}}$ and $w^{\mathrm{fb}}_{\omega,\mathrm{VB}}$ are the height and width of the bounding box, respectively. The position of a vascular bundle is defined by its morphological center, corresponding to the center of the bounding box. Considering the complexity of vascular bundle morphology, it is recommended by the authors to describe the cross-sectional shape directly on image data denoted by $s^{\mathrm{fb}}_{\omega,\mathrm{VB}}[m,n]$. Therefore the extracted vascular bundle images are shifted, so that the morphological center lies in the image center. Then the images are rotated into a vertical orientation, scaled to a fiber bundle volume fraction of 15% and reshaped to fixed image size of 128 × 128 pixels. This normalization process ensures that the shape-describing images are invariant to fluctuations in vascular bundles size, orientation and position.

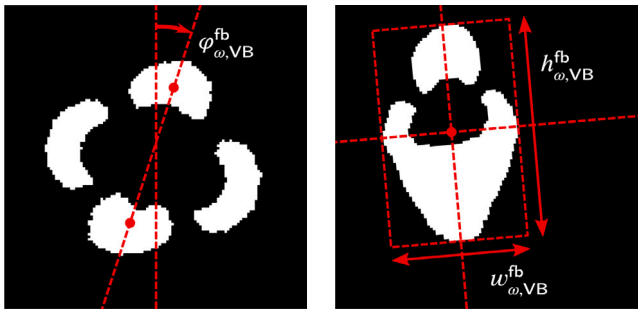

(a) VB1 Orientation (b) Morphological Center

Fig. 4. Measuring of the orientation of a vascular bundle using the centroids of the uppermost and lowermost fiber bundle (a). Morphological center of a vascular bundle defined by the bounding box aligned with vascular bundle orientation (b)

Image-based characterization

Based on the predicted vascular bundle types, the overall indicator image is partitioned into three type-specific indicator images $I^{\mathrm{fb},i}_{\omega}[m,n]$ with $i = \mathrm{VB1}, \mathrm{VB2}, \mathrm{VB3}$. Using Eqs. (5) and (6), the discrete type-specific parameter functions are derived for each vascular bundle type individually and are referred to as parameter images $\underline{Z}^{\mathrm{fb},i}_{\omega}[m,n]$. It is noteworthy that, in contrast to the indicator images, truncated vascular bundles located at the horizontal boundaries of the image are excluded from the construction of the parameter images. As described in Section 1.1 the variation of morphology and density of the uniaxial orientated vascular bundles is negligible in circumferential direction. Hence, in accordance with literature [8,24,25], the mesostructure is assumed to be statistically homogeneous and ergodic in both the longitudinal and circumferential direction. As a consequence each vertical pixel column of the indicator and parameter images represent a realization of the mesostructure. Moreover Eq. (18) holds in circumferential direction and the ensemble and phase average also consider averaging over the horizontal pixel rows. By scaling all images to a uniform vertical pixel count, e.g. the maximum height within the ensemble, and stacking them along the vertical axis, the type-specific indicator and parameter functions are each combined into single images denoted by $I^{\mathrm{fb},i}[m,n]$ and $\underline{Z}^{\mathrm{fb},i}[m,n]$, respectively. Consequently, information regarding the absolute wall thickness of individual realizations is no longer retained. Instead, a normalized radial coordinate $\tilde{r}$ is introduced, defined as 0 at the inner bound and 1 at the outer bound of the culm wall, as shown in Fig. 3. According to Eqs. (8), (12) and (13), the type-specific

characteristics are computed by applying the ensemble and phase average to the stacked, type-specific indicator and parameter images in vertical direction. As a result, the characteristics of the bamboo mesostructure are only dependent on the radial position and, in this two-dimensional case, are reduced to the fiber bundle area fractions $a^{\mathrm{fb},i}(\tilde{r})$ such as the average and standard deviation of vascular bundle morphology $\underline{\mu}^{\mathrm{fb},i}(\tilde{r})$ and $\underline{\sigma}^{\mathrm{fb},i}(\tilde{r}) = \sqrt{\underline{k}^{\mathrm{fb},i}(\tilde{r})}$, respectively. Since all morphological parameters, including vascular bundle orientation, are treated as scalars, the standard deviation is computed as the square root of the covariance of the vascular bundle morphology. It is important to note that statistical analysis of orientation expressed as an angle yields different results compared to its representation as an orientation tensor due to their nonlinear relationship. Considering a cylindrical internode with an inner and outer radius, r_i and r_o, respectively, Eqs. (17) for the volume-average d characteristics of the entire cross-section of the culm wall are reduced to

$$a_{\mathrm{cw}}^{\mathrm{fb},i} = \frac{2}{r_\mathrm{o}^2 - r_\mathrm{i}^2} \int_{r_\mathrm{i}}^{r_\mathrm{o}} a^{\mathrm{fb},i}(\tilde{r}) r \,\mathrm{d}r, \tag{22}$$

$$\underline{\mu}_{\mathrm{cw}}^{\mathrm{fb},i} = \frac{2}{r_\mathrm{o}^2 - r_\mathrm{i}^2} \int_{r_\mathrm{i}}^{r_\mathrm{o}} \frac{a^{\mathrm{fb},i}(\tilde{r})}{a_{\mathrm{avg}}^{\mathrm{fb},i}} \underline{\mu}^{\mathrm{fb},i}(\tilde{r}) r \,\mathrm{d}r, \tag{23}$$

$$\underline{\sigma}^{\mathrm{fb},i}{}_{\mathrm{cw}}^{\,2} = \frac{2}{r_\mathrm{o}^{\,2} - r_\mathrm{i}^2} \int_{r_\mathrm{i}}^{r_\mathrm{o}} \frac{a^{\mathrm{fb},i}(\tilde{r})}{a_{\mathrm{avg}}^{\mathrm{fb},i}} \underline{\sigma}^{\mathrm{fb},i}(\tilde{r})^2 r \,\mathrm{d}r, \tag{24}$$

$$n_{\mathrm{cw}'}^{\mathrm{fb},i} = \frac{2}{r_\mathrm{o}^2 - r_\mathrm{i}^2} \int_{r_\mathrm{i}}^{r_\mathrm{o}} n^{\mathrm{fb},i}(\tilde{r}) r \,\mathrm{d}r. \tag{25}$$

Measuring of vascular bundle domain and density

The number density of vascular bundles $n_{\mathrm{fb}}(\tilde{r})$ is not an independent characteristic of the mesostructure and is given by Eq. (15). However, the number density is also measured directly from the spatial distribution of the vascular bundles using Laguerre tessellations for comparison. According to Imai et al. [59] a Laguerre tessellation is a weighted Voronoi tessellation which is defined by a set of seeds $\boldsymbol{x}_i$ and corresponding set of weights w_i. For an individual tessellation cell C_i of a euclidean space Ω holds

$$C_i = \left\{ \boldsymbol{x} \in \Omega | d(\boldsymbol{x}, \boldsymbol{x}_i)^2 - w_i \le d(\boldsymbol{x}, \boldsymbol{x}_j)^2 - w_j, i \ne j \right\}, \tag{26}$$

where $d(\boldsymbol{x}, \boldsymbol{x}_i)$ is the euclidean distance according to the periodic or non-periodic bounds of Ω. As shown in Fig. 3(e), for each realization a two dimensional Laguerre tessellation is computed using the morphological centers of the detected vascular bundles as seeds. In this work, the weight of the kth vascular bundle of realization ω is chosen as $w_k = 0.8(A_k^{\mathrm{fb}} - \min(A_i^{\mathrm{fb}}))$ to ensure that the vascular bundle lies inside the corresponding tessellation cell, which is called the vascular bundles domain. The domain area is given by $D_{\omega,\mathrm{VB}}^{\mathrm{fb}} = |C_i|$ and is also accounted for as morphology parameter. Hence, it is included in the characterization framework described earlier. Because the overall average domain area $\bar{D}^{\mathrm{fb}}(\tilde{r})$ gives the area related to one vascular bundle, its inverse gives the number of vascular bundles per area unit. According to Section 2.1 this defines the vascular bundle number density of the fiber bundle phase. Hence, for the overall and type-specific number density holds

$$n^{\mathrm{fb}}(r) = \frac{1}{\bar{D}^{\mathrm{fb}}(r)}, \qquad n^{\mathrm{fb},i}(r) = \frac{\phi^{\mathrm{fb},i}(r)}{\bar{D}^{\mathrm{fb},i}(r)}. \tag{27}$$

Because the fiber bundles and the vessels are both part of a vascular bundle and never occur separated from each other, the number density of the fiber bundle phase and the number density of the vessel phase are assumed to be equal.

2.3. Reconstruction of bamboo mesostructure

Vascular bundle sampling and configuration

Regarding the homogenization approach for the statistically homogeneous mesostructure described in Section 2.4, ergodic and periodic surrogate models representing the local characteristics at a given normalized radial position $\tilde{r}$ are considered. The reconstruction process of local surrogate models follows algorithm 1 and is described below. A periodic unit cell $Q = [0, Q_1] \times [0, Q_2]$ is considered, where the axis 1 and 2 are aligned with the radial and circumferential directions, respectively. Thus, the out-of-plane axis is the longitudinal direction, in which the mesostructure is invariant. The unit cell should contain $N^{\mathrm{fb},i}$ vascular bundles of type $i = \mathrm{VB1}, \mathrm{VB2}, \mathrm{VB3}$ in a non-overlapping configuration. The morphology of the kth ($k = 1, \ldots, N^{\mathrm{fb},i}$) vascular bundle of type i is denoted by a set of parameters $\underline{z}_k^{\mathrm{fb},i}$ including the cross sectional fiber bundle area $A_k^{\mathrm{fb},i}$, shape $s_k^{\mathrm{fb},i}$ and orientation $\varphi_k^{\mathrm{fb},i}$. Regarding a given radial position r, the vascular bundle morphologies are sampled from a normal distribution $\mathcal{N}$ defined by the characteristic average $\underline{\mu}^{\mathrm{fb},i}(r)$ and standard deviation $\underline{\sigma}^{\mathrm{fb},i}(r)$. The samples are generated by mapping a quasi-random Sobol sequence into a normal distribution, then rescaled using an affine transformation to match the target characteristics. To match the total fiber bundle area fraction $a^{\mathrm{fb}}(r)$, the number of type i vascular bundles is computed by $N^{\mathrm{fb},i} = n^{\mathrm{fb},i}(r) Q_1 Q_2$ considering the type specific number fraction. To find a non-overlapping configuration of the vascular bundles, their polyhedral domains defined by tessellation are considered. Hence, a periodic Laguerre tessellation is computed inside the unit cell, which is stretched in circumferential direction by the factor $\bar{\alpha}^{\mathrm{fb}}(r)$ denoting the average aspect ratio of the vascular bundle cross-section. As described in Section 2.2, this factor is computed from the bounding box of the

Algorithm 1 Reconstruction process of bamboo mesostructure

Input: normalized position $\tilde{r}$, unit cell size $[Q_1, Q_2]$, pixel edge length h

Sampling:
- $N^{\mathrm{fb},i} \leftarrow n^{\mathrm{fb},i}(r) Q_1 Q_2$ ▷ type-specific VB number
- **for** $i \leftarrow 1, 3$ **do**
  - **for** $k \leftarrow 1, N^{\mathrm{fb},i}$ **do**
    - $\underline{z}_k^{\mathrm{fb},i} \sim \mathcal{N}(\underline{\mu}^{\mathrm{fb},i}(r), \underline{\sigma}^{\mathrm{fb},i}(r)^2)$ ▷ quasi-random sampling
    - $A_k^{\mathrm{fb},i}, \varphi_k^{\mathrm{fb},i}, s_k^{\mathrm{fb},i} \leftarrow \underline{z}_k^{\mathrm{fb},i}$
    - $D_k^{\mathrm{fb},i} \leftarrow A_k^{\mathrm{fb},i} / a^{\mathrm{fb}}(r)$
  - **end for**
- **end for**

Seeding:
- $\bar{\alpha}^{\mathrm{fb}} \leftarrow$ bounding box ratio of $\tilde{s}^{\mathrm{fb}}(r)$
- Transform Cell: $Q_2 \leftarrow Q_2 \bar{\alpha}^{\mathrm{fb}}$ ▷ stretching along axis 2
- Compute centroidal tessellation with domain sizes $D_k^{\mathrm{fb},i}$ ▷ [40]
- Transform Cell: $Q_2 \leftarrow Q_2 / \bar{\alpha}^{\mathrm{fb}}$
- $\boldsymbol{x}_k^{\mathrm{fb},i} \leftarrow$ centroids of tessellation domains

Image generation:
- $\mathcal{I}[m, n] = 0$, with $m = 1, \ldots, Q_1/h, n = 1, \ldots, Q_2/h$
- **for** $i \leftarrow 1, 3$ **do**
  - **for** $k \leftarrow 1, N^{\mathrm{fb},i}$ **do**
    - $A \leftarrow A_k^{\mathrm{fb},i}/h^2 - \sum \mathcal{I} + \sum_{l=1}^{k-1} A_l^{\mathrm{fb},i}/h^2$ ▷ area fraction control
    - $s \leftarrow \mathtt{resize}(s_k^{\mathrm{fb},i}, A)$ ▷ resize image with $\sum s = A$
    - $s \leftarrow \mathtt{rotate}(s, \varphi_k^{\mathrm{fb},i})$ ▷ rotate image by $\varphi_k^{\mathrm{fb},i}$
    - $\mathcal{I} \leftarrow \mathtt{insert}(s, x_k^{\mathrm{fb},i}/h)$ ▷ only where $s \ne 0$
  - **end for**
- **end for**

overall average vascular bundle shape $\bar{s}^{\mathrm{fb}}(r)$. Following the approach of Kuhn et al. [40], the seeds and weights of the tessellation within the stretched unit cell are optimized to generate centroidal domains, i.e. the seeds equal the domain centroids, and to match the domain size distribution $D_k^{\mathrm{fb},i}\bar{a}^{\mathrm{fb}}$, whereas the domain size distribution in the unstretched unit cell is given by $D_k^{\mathrm{fb},i} = A_k^{\mathrm{fb},i}/a^{\mathrm{fb}}(r)$. Because the tessellation algorithm cannot account for a prescribed aspect ratio and orientation distribution of the domains, the standard deviation of vascular bundle shape and orientation $\hat{\varphi}^{\mathrm{fb},i}(r)$ are forced to be zero. Hence the mentioned stretching procedure of the unit cell is used to prescribe a uniform domain aspect ratio. This results in a centroidal tessellation of the unstretched unit cell that reflects the morphological texture associated with the average vascular bundle aspect ratio. Finally, the centroids of the domains in the unstretched unit cell are set to the geometric centers of the vascular bundles $\boldsymbol{x}_k^{\mathrm{fb},i}$, ensuring that each bundle fits within its respective domain and does not overlap with others.

Generation of mesostructure images

The continuous representation of the unit cell is discretized into an image $\mathcal{I}[m,n]$ with a given pixel edge length h and pixel indices $m = 1,\dots,Q_1/h$ and $n = 1,\dots,Q_2/h$. As a first step, binary images of the individual vascular bundles are generated. To do so, the vascular bundle shape, described by image data, is scaled to match the pixel size regarding the fiber bundle area $A_k^{\mathrm{fb},i}$ and rotated according the orientation $\varphi_k^{\mathrm{fb},i}$. Then, the images of the individual vascular bundles are inserted into the unit cell image according to the seeded positions $\boldsymbol{x}_k^{\mathrm{fb},i}$. During the sequential insertion of the vascular bundle images, the discretization error regarding the total fiber area fraction is monitored. To minimize the error, the fiber bundle area of the current vascular bundle to be inserted is updated according to the current error. This leads to a discrepancy of the generated and the targeted vascular bundle size distribution. However, Schneider [60] shows for fiber-reinforced composites that the homogenized effective stiffness is more sensitive to a variation of fiber volume fraction than to a variation of the fiber morphology.

For higher fiber bundle area fractions above 60% the described tessellation method is not sufficient to generate a complete non-overlapping configuration of the vascular bundles. In this case, some vascular bundles penetrate their domains, which could lead to a potential overlap with neighboring bundles. If an overlap is detected during the insertion, the vascular bundle is successively shifted and contracted until a non-overlapping configuration is found. This procedure also effects the discretization error of the total fiber bundle are fraction and therefore interacts with the error minimization as well as enlarges the deviation from the target vascular bundle size distribution. However, a non-overlapping configuration is preferred because an overlapping arrangement would result in an even stronger deviation from the observed realizations of the mesostructure and would significantly distort the prediction of effective macroscopic properties.

2.4. Micromechanical homogenization methods

Scale-bridging of statistically inhomogeneous media

In this work, only linear elastic material behavior is considered on the mesoscopic scale. Following Al-Rukaibawi et al. [49], fiber bundles and parenchyma matrix are modeled to be perfectly bonded and elastically isotropic, represented by the stiffness tensors $\mathbb{C}_{\mathrm{fb}}$ and $\mathbb{C}_{\mathrm{m}}$, respectively. The corresponding elastic properties are summarized in Table 2. Considering the cellular microstructure of the fiber bundles and the matrix material, the presented modeling approach provides only an approximate representation of their anisotropic nature. Despite this simplification on micro scale, the macroscopic anisotropy of the bamboo culm wall is captured by the morphological features on meso scale, i.e., the inclusion shape and distribution. Hence, the mechanical behavior of the culm wall is determined by employing homogenization methods that bridge the gap between mesoscopic and macroscopic scales incorporating local structural anisotropy. For a homogeneous surrogate model of a given heterogeneous microstructure to be representative, the power equivalency given by the Hill–Mandel condition needs to be fulfilled, which reduces to a strain energy equivalency in the linear elastic case. This holds for ergodic media with scale separation, whereby the surrogate is derived from a representative volume element with, e.g., periodic boundary conditions.

Considering a statistically inhomogeneous microstructure with sufficiently small macroscopic gradients of the microstructural characteristics, the ergodic hypotheses approximately holds at macroscopic material points and local periodic surrogate models can be used to approximate the inhomogeneous macroscopic behavior. In this case, first-order homogenization can be applied, which solves a locally defined microstructural problem in order to derive a macroscopic constitutive law of first order. Other homogenization approaches are described in Section 1.

In bamboo, where fiber bundles and culm wall dimensions are of the same order of magnitude, a separation between the mesoscopic and the macroscopic scale is not given. However, scale separation is assumed as an approximation in order to apply the local approach as shown in Fig. 5, which enables robust numerical implementation and efficient computation while still capturing the dominant effective material trends. Accordingly, the macroscopic stiffness $\bar{\mathbb{C}}$ of the bamboo culm wall is derived by employing mean- and full-field methods informed by mesostructural data, as described in the following paragraphs.

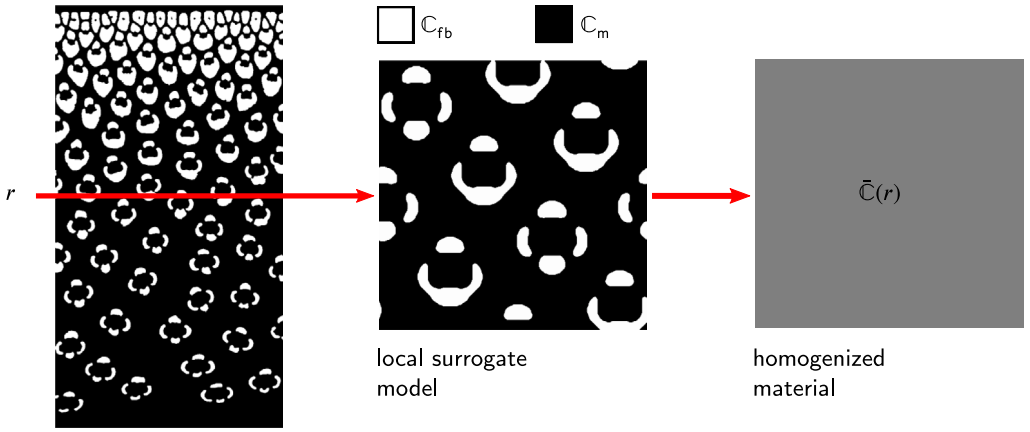

Fig. 5. First-order homogenization approach for the statistically inhomogeneous mesostructure of bamboo. The effective macroscopic behavior at a given radial position r is derived by the homogenization of a ergodic and periodic surrogate model representing the structural characteristics at r.

Table 2
Linear elastic properties of matrix material and fiber bundles according to [8] (a), [47] (b) and [49] (c). Due to lacking data, the Poisson ratios are the mean of values reported in studies (b) and (c).

	Fiber bundle	Matrix material	References
E in GPa	39.8	1.93	(a)
ν in –	0.25	0.37	(b), (c)

Mean-field homogenization

In order to describe the homogenization problem, local strain and stress fields, denoted by $\boldsymbol{\varepsilon}(\boldsymbol{x})$ and $\boldsymbol{\sigma}(\boldsymbol{x})$, respectively, are considered inside the surrogate model. Because the Hill–Mandel condition holds, the effective macroscopic strain and stress are given by the volume average of the local fields, $\bar{\boldsymbol{\varepsilon}} = \langle \boldsymbol{\varepsilon}(\boldsymbol{x}) \rangle$ and $\bar{\boldsymbol{\sigma}} = \langle \boldsymbol{\sigma}(\boldsymbol{x}) \rangle$, respectively. In the linear elastic case the homogenized macroscopic stiffness is given exactly by

$$\bar{\mathbb{C}} = \langle \mathbb{C}(\boldsymbol{x}) \mathbb{A}(\boldsymbol{x}) \rangle \tag{28}$$

with the local stiffness $\mathbb{C}(\boldsymbol{x})$. The strain localization tensor is denoted by $\mathbb{A}(\boldsymbol{x})$ and implicitly given by $\boldsymbol{\varepsilon}(\boldsymbol{x}) = \mathbb{A}(\boldsymbol{x})[\bar{\boldsymbol{\varepsilon}}]$. If only two piecewise constant phases $\mathbb{C}_1$ and $\mathbb{C}_2$ are given, for the effective stiffness holds

$$\bar{\mathbb{C}} = \mathbb{C}_1 + v_2(\mathbb{C}_2 - \mathbb{C}_1)\langle \mathbb{A}(\boldsymbol{x}) \rangle_2, \tag{29}$$

where v_2 is the volume fraction and $\langle \cdot \rangle_2$ is the volume average of the second phase. Full-field methods solve the boundary value problem on the micro scale to access the local fields, from which the exact strain localization tensor can be derived. In mean-field homogenization the strain localization tensor is approximated considering only the constituent properties and microstructural statistics, i.e. the characteristics of the microstructure. The most common methods are derived from the Singular Approximation, which is first formulated by Fokin [61] and based on the single inclusion problem of Eshelby [62]. The Singular Approximation can be motivated by replacing the actual microstructure with an ensemble of Eshelby problems where each of the local phases is modeled as an inclusion embedded in a linear elastic reference material $\mathbb{C}_0$. According to Willis [63], this approach is a generalization of the results of Hashin and Shtrikman [34]. The solution for the strain localization tensor of the constituent phases is given by Walpole [64] as

$$\begin{aligned} \mathbb{A}(\boldsymbol{x}; \mathbb{C}_0) &= \mathbb{L} \langle \mathbb{L} \rangle^{-1}, \\ \mathbb{L}(\boldsymbol{x}; \mathbb{C}_0) &= \left(\mathbb{I}^{\mathrm{S}} + \mathbb{P}_0 \left(\mathbb{C}(\boldsymbol{x}) - \mathbb{C}_0 \right) \right)^{-1}, \end{aligned} \tag{30}$$

where $\mathbb{P}_0$ is Hill's polarization tensor for ellipsoidal inclusions [63]. The reference material is a free parameter of the Singular Approximation and can be described as a measure for the strain deviation between the actual phases of the microstructure. Morawiec [65] demonstrates that the choice of the reference material affects the derivation of different homogenization methods. In the limit $\mathbb{C}_0 \to 0$ there is no interaction between the inclusions, which means they can deform freely and the stresses are equal. Therefore, the Singular Approximation leads to the harmonic average of the constituent stiffnesses

$$\bar{\mathbb{C}}^{\mathrm{R}} = \langle \mathbb{C}(\boldsymbol{x})^{-1} \rangle^{-1} = \left(\mathbb{C}_1^{-1} + v_2 \left(\mathbb{C}_2^{-1} - \mathbb{C}_1^{-1} \right) \right)^{-1}, \tag{31}$$

first formulated by Reuss [66]. The limit $\mathbb{C}_0 \to \infty$ implies the equality of the strains inside all phases and the Singular Approximation tends to the arithmetic average originally derived by Voigt [67] as

$$\bar{\mathbb{C}}^{\mathrm{V}} = \langle \mathbb{C}(\boldsymbol{x}) \rangle = \mathbb{C}_1 + v_2 \delta\mathbb{C}, \tag{32}$$

where $\delta\mathbb{C} = \mathbb{C}_2 - \mathbb{C}_1$ is the material contrast. It can be shown, that the Voigt and Reuss model serve as physical bounds on the effective stiffness, where $\bar{\mathbb{C}}^{\mathrm{R}}$ is the lower and $\bar{\mathbb{C}}^{\mathrm{V}}$ is the upper bound. Following Lobos and Böhlke [68], adopting the zeroth-order bounds corresponding to the constituent phases as reference material leads to the lower and upper bounds of Hashin and Shtrikman [34], expressed for the given case as

$$\bar{\mathbb{C}}^{\mathrm{HS}-} = \mathbb{C}_1 + v_2 \delta\mathbb{C} \left[\mathbb{I}^{\mathrm{S}} + (1 - v_2) \mathbb{P}_1 \delta\mathbb{C} \right]^{-1}, \tag{33}$$

$$\bar{\mathbb{C}}^{\mathrm{HS}+} = \mathbb{C}_2 - (1 - v_2) \delta\mathbb{C} \left[\mathbb{I}^{\mathrm{S}} - v_2 \mathbb{P}_2 \delta\mathbb{C} \right]^{-1}. \tag{34}$$

respectively. In this case of two piecewise constant, isotropic phases the lower Hashin–Shtrikmann bound equals the approximation of Mori and Tanaka [33]. For the Self Consistent Model introduced by Kröner [69] the effective stiffness is chosen for the reference material, leading to a implicit formulation

$$\bar{\mathbb{C}}^{\mathrm{SC}} = \mathbb{C}_1 + v_2(\mathbb{C}_2 - \mathbb{C}_1)\langle \mathbb{A}(\boldsymbol{x}; \bar{\mathbb{C}}^{\mathrm{SC}}) \rangle_2, \tag{35}$$

which can be solved numerically using an iterative fixed point scheme. To apply the mean-field models to the local surrogate model of the bamboo mesostructure, phases 1 and 2 are considered to be the parenchyma matrix and the fiber bundle phase, respectively. The volume fractions are given naturally after the characterization described in Section 2.2. For the Hashin–Shtrikmann bounds and the Self Consistent model, the fiber bundles of a vascular bundle are modeled as a unidirectional cylinder. Hill's polarization tensor for such a needle-shaped particle is given in Appendix D.

FFT-based homogenization

The FFT-based homogenization method performs full-field simulations on a volume element subjected to a prescribed macroscopic strain $\bar{\boldsymbol{\varepsilon}}$. The approach follows the formulation introduced by Moulinec and Suquet [70], which iteratively solves the Lippmann–Schwinger equation on a regular Cartesian grid. The local strain field is discretized using trigonometric polynomials that act as Fourier basis functions. This spectral discretization makes the method particularly suitable for periodic boundary conditions. Differential operators are applied in the frequency domain, eliminating the need to assemble and invert a global system matrix as in finite element methods. The FFT-algorithm enables efficient transitions between real and frequency space for convolution and differential operations. To minimize oscillations in the solution field the staggered grid discretization introduced by Schneider et al. [71] is used. As iterative solver the conjugate gradient method proposed by Zeman et al. [72] is chosen, especially suited for linear problems. From the derived local fields, the macroscopic stress $\bar{\boldsymbol{\sigma}}$ is computed by volume averaging. By performing six simulations with different prescribed macroscopic strain modes, the effective stiffness $\bar{\mathbb{C}}^{\mathrm{FFT}}$ is derived according to the macroscopic stress response. Further details on the approach can be found in Schneider [39].

The FFT-based homogenization is applied to the local surrogate models of the bamboo mesostructure. In this case, the surrogate models are realized as representative images reconstructed according to the local characteristics. The reconstruction process is described in Section 2.3. Relying on resolution and representativity studies discussed in Appendix E, the image resolution h and the cell edge length Q of the surrogate models are chosen to be 2 µm and 3mm, respectively, for any radial position.

3. Results and discussion

3.1. Characteristics of the bamboo mesostructure

Fiber bundle area fraction

The measured radial distributions of the overall and type-specific fiber bundle area fractions are presented in Fig. 6(a). The overall area fraction increases from approximately 10% in the inner region to a maximum of 77.62% in the outer region of the culm wall. This trend is consistent with observations reported in the literature [8,15], and reflects the properties of a statistically inhomogeneous microstructure. Notably, the observed maximum local area fraction exceeds values reported in previous studies, which can be attributed to the higher

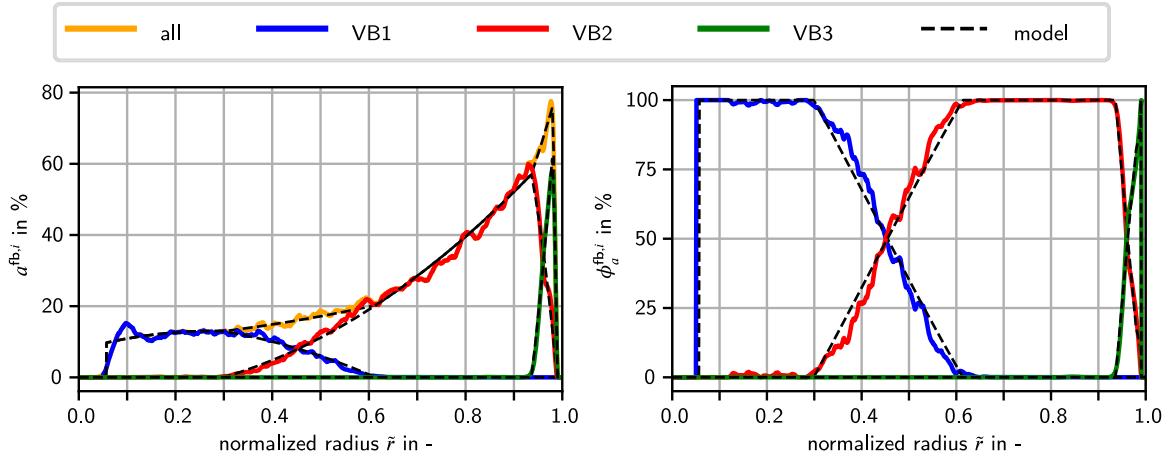

(a) Fiber bundle area fraction

(b) Type fractions

Fig. 6. Measured and modeled radial distributions of the fiber bundle domain area fractions (a) and type fractions (b) for different vascular bundle types.

spatial resolution of the present dataset, enabling the capture of finer structural details. Using Eq. (22) and the average internode geometry provided in Table 1, the volume average of overall area fraction is calculated to be 24.11%. This value aligns well with findings from previous studies, such as 23.68% reported by Li et al. [21] and 25.5% by Xu et al. [24], indicating that the segmentation algorithm, highly sensitive to area fraction estimation, performs with sufficient accuracy. The volume average of area fractions for fiber bundle types VB1, VB2, and VB3 are 5.03%, 17.31%, and 1.77%, respectively. Based on their radial distributions and the resulting area-specific type fractions shown in Fig. 6(b), six distinct regions can be identified across the culm wall. These include two outermost layers—the pith and the skin—where no vascular bundles are present. Between these are four intermediate layers, ordered from inner to outer: a region containing only VB1 bundles, a transition layer from VB1 to VB2, followed by a region dominated by VB2 bundles and a transition layer from VB2 to VB3. The relative thicknesses of these six layers, from the innermost to the outermost, are 5.64%, 24.23%, 31.52%, 32.23%, 5.38%, and 1.01%, respectively. To model the type-specific area fraction distributions, piecewise quadratic functions were fitted using the least-squares method, with continuity conditions enforced at the boundaries between the intermediate layers. The resulting model parameters are summarized in Appendix F. The overall area fraction model, derived using Eq. (16), accurately reproduces the measured distribution, as illustrated in Fig. 6(a).

Fiber bundle morphology of a vascular bundle

The radial distribution of the fiber bundle area within individual vascular bundles is illustrated in Fig. 7(a). The overall trend shows an increase in fiber bundle area with normalized radius, followed by a decline beyond approximately $\tilde{r} = 0.8$. A comparison of the average areas reveals that type VB2 vascular bundles are statistically larger than VB1 and VB3 bundles within their respective transition layers, indicating a distinct size differentiation among bundle types. To model the radial distribution of the type-specific average fiber bundle area, piecewise fourth-order polynomial functions are employed. The model parameters are obtained by fitting the polynomial functions to the measured average values, explicitly accounting for the layer boundaries identified in the analysis of the type distribution. The resulting model parameters are summarized in Appendix F. The standard deviation for each bundle type is assumed to be constant within the layers where the respective type occurs, and is defined as the volume average of the measured standard deviations computed by Eq. (24). The values are $0.82\times10^{-2}\,\mathrm{mm}^{-2}$ for VB1, $0.96\times10^{-2}\,\mathrm{mm}^{-2}$ for VB2 and $0.79\times10^{-2}\,\mathrm{mm}^{-2}$ for VB3. As shown in Fig. 7(a), the modeled distributions closely match the experimental data, demonstrating the effectiveness of the polynomial approach in capturing the radial variation of fiber bundle area. As shown in Fig. 7(b), the radial distribution of the average vascular bundle orientation is approximately constant and can be modeled as zero for all types. The standard deviation of the measured orientation varies slightly over the radius and is given by an volume average of 9,93°, 7.85° and 10.36° for vascular bundles of type VB1, VB2 and VB3, respectively.

Fig. 7(c) illustrates the measured average fiber bundle shape of vascular bundles at four different normalized radial positions, i.e. $\tilde{r}_\mathrm{A} = 0.2$, $\tilde{r}_\mathrm{B} = 0.5$, $\tilde{r}_\mathrm{C} = 0.8$ and $\tilde{r}_\mathrm{D} = 0.95$. At the radial positions, where two types are present, there is a significant morphological difference between the vascular bundle types. To model the average fiber bundle shape, binary images are generated through post-processing of the measured image data. For an arbitrary normalized radial position $\tilde{r}$, two shape images $s_k^{\mathrm{fb,i}}$ and $s_{k+1}^{\mathrm{fb,i}}$ are identified within the dataset, corresponding to neighboring radial positions $\tilde{r}_k < \tilde{r}$ and $\tilde{r}_{k+1} > \tilde{r}$. These images serve as the basis for interpolating the fiber bundle shape at $\tilde{r}$. The interpolated images are symmetrized along the horizontal axis to ensure geometric consistency. To suppress small-scale oscillations present in the measured shape images, a median filter with a cross-shaped kernel is applied. Finally, a simple image segmentation using a threshold of 50% is performed to derive binary shape representations for each vascular bundle type at the given radial position. As illustrated in Fig. 7(c), the modeled shapes are represented by the fiber bundle contours and capture the measured average fiber bundle geometry exceptionally well.

Vascular bundle arrangement

The arrangement of vascular bundles was analyzed by applying Laguerre tessellation to mesostructural realizations, which were used to define the domains associated with individual vascular bundles. Fig. 8(a) presents the radial distribution of the average and standard deviation of the domain area, differentiated by bundle type. The results indicate an initial increase in average domain area, reaching approximately $0.6\,\mathrm{mm}^2$ at a normalized radial position of $\tilde{r} = 0.2$, followed by a roughly linear decrease with increasing radius. No statistically significant differences are observed between the domain areas of vascular bundle types VB1 and VB2. In contrast, VB3 domains are consistently smaller, particularly within the outer transition layer. Using Eqs. (16) and (27), the overall and type-specific number density of vascular bundles was derived from the measured domain area distribution. As shown in Fig. 8(b), the overall number density remains approximately constant at $1.8\,\mathrm{mm}^{-2}$ within the inner half of the culm wall and increases significantly with the normalized radius in the outer half, following a strongly nonlinear trend. Using Eq. (25) and the average internode geometry provided in Table 1, the volume average of the

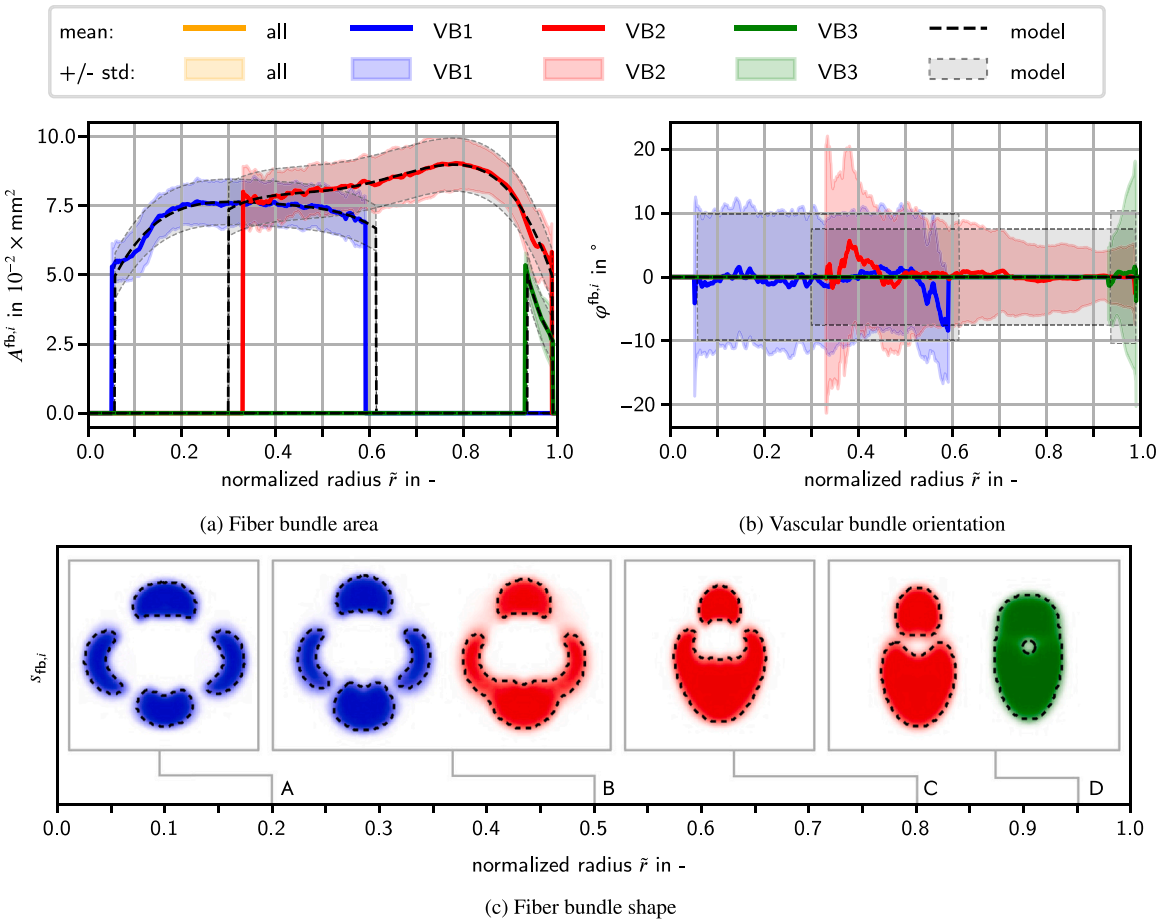

(a) Fiber bundle area

(b) Vascular bundle orientation

(c) Fiber bundle shape

Fig. 7. Measured and modeled radial distributions of the type-specific vascular bundle morphology parameterized by the fiber bundle area (a), vascular bundle orientation (b) and cross-sectional shape (c). The statistical variation are represented as the range of one standard deviation around the average distribution.

number density results in 3.37 mm^{-2} overall, and 0.7 mm^{-2}, 2.14 mm^{-2}, and 0.53 mm^{-2} for vascular bundle types VB1, VB2, and VB3, respectively. These findings are consistent with the results reported by Li et al. [21], and suggest that the mesostructure is predominantly composed of vascular bundles of type VB2.

To model the radial distribution of the type-specific number density, Eq. (15) is applied to the modeled type-specific fiber bundle area fraction and the fiber bundle area of a vascular bundle. The type-specific domain distribution is modeled using Eq. (27). As shown in Figs. 8(a) and 8(b), the theoretical models reproduce the measured distributions with high accuracy. In the vicinity of the outer skin layer, the model for VB3 vascular bundles tends to underestimate the measured number density. This discrepancy is attributed to limitations in domain measurement using tessellation. Fig. 9(a) illustrates that the domains of a tessellated realization near the outer boundary do not fully enclose the corresponding vascular bundles and fail to capture the aspect ratio of their cross sections. As a result, the domains, particularly those associated with VB3, are too small to accurately represent the spatial arrangement of the vascular bundles relative to their neighbors. Consequently, the measured number density in this region is overestimated.

The observations indicate that the spatial arrangement of vascular bundles in the bamboo mesostructure corresponds to a densely packed configuration with a regular pattern, as evidenced by the low variance in domain sizes. The authors propose modeling this regular arrangement using a grid-based approach, illustrated in Fig. 9(b). By connecting vascular bundles to regularly positioned neighbors, starting from the innermost entities, grid lines can be identified that run angular with respect to the radial direction and extend across the entire culm wall. Since the number density increases with radial position, not all vascular bundles are intersected by continuous grid lines. Therefore, truncated lines are introduced to connect the remaining angular rows. The number of these truncated grid lines increases in accordance with the density distribution. This modeling approach results in a grid structure that reflects both the regular spatial arrangement and the radial increase in vascular bundle number density.

3.2. Representative images of the bamboo mesostructure

Using the reconstruction algorithm described in Section 2.3, and based on the modeled characteristics of the bamboo mesostructure derived in Section 3.1, representative images of the mesostructure at selected radial positions are generated. Fig. 10 presents four representative realizations corresponding to the normalized radial positions $\tilde{r}_{\mathrm{A}} = 0.2$, $\tilde{r}_{\mathrm{B}} = 0.5$, $\tilde{r}_{\mathrm{C}} = 0.8$ and $\tilde{r}_{\mathrm{D}} = 0.95$. According to the numerical studies outlined in Appendix E, the pixel edge length and the edge length of the quadratic unit cell are set to $h = 2$ µm and $Q = 3$ mm, respectively. These parameters ensure that the numerical error in the computation of the effective stiffness at the specified positions remains below 1%. In contrast to the mesostructural model presented by Al-Rukaibawi et al. [49], which considers only a single vascular bundle, the representative images generated in this study incorporate a higher degree of structural detail. This is enabled by the advanced characterization and reconstruction framework employed, allowing for a more comprehensive representation of the mesostructural characteristic. A comparison between the local structural models and an actual realization of the bamboo mesostructure reveals that the reconstructed images qualitatively resemble the real structure, particularly at radial positions where the gradient in mesostructural characteristics is low.

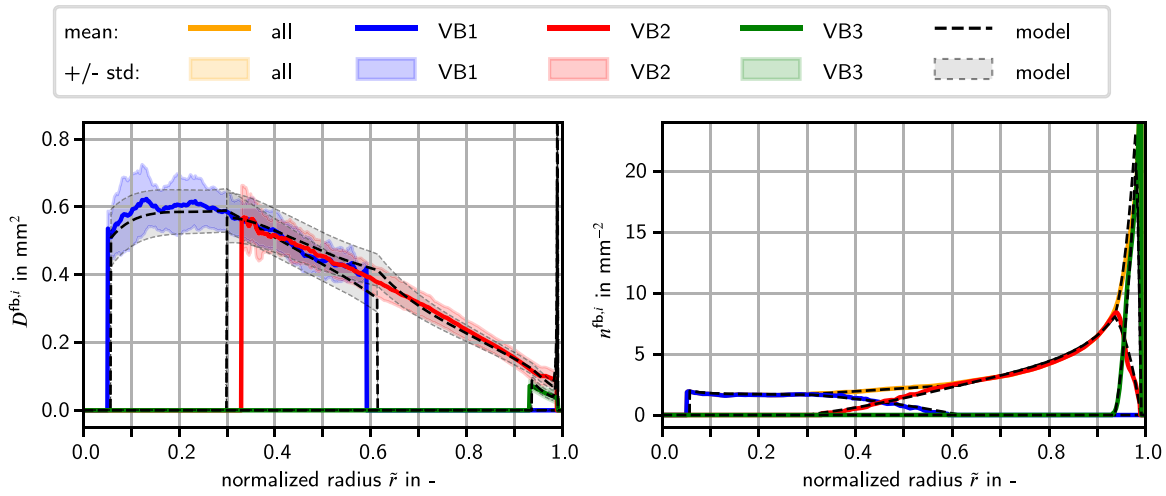

(a) VB domain area

(b) VB number density

Fig. 8. Measured and modeled radial distributions of the vascular bundle domain area (a) and number density (b) for different vascular bundle types. The statistical variation are represented as the range of one standard deviation around the average distribution.

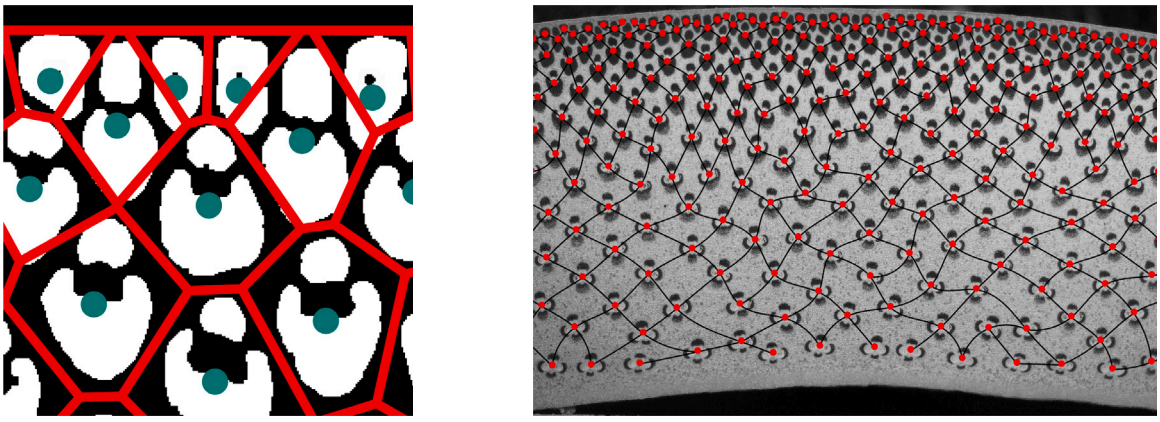

(a) Tessellation near outer skin

(b) Grid model for vascular bundle arrangement.

Fig. 9. Tessellation of the bamboo mesostructure near the outer skin based on the morphological centers of vascular bundles (a). Grid model for vascular bundles reflecting the regular spatial arrangement and the radial increase in vascular bundle number density (b).

Near the outer skin of the culm wall, the same vascular bundle types are observed in both the model and the actual structure. However, the spatial arrangement of vascular bundles in the reconstructed images does not reflect the arrangement found in the realization. Specifically, in the actual structure, vascular bundles of type VB3 occur exclusively above those of type VB2, whereas in the model, the vascular bundles are distributed statistically homogeneous without positional constraints.

To quantitatively evaluate the accuracy of the reconstruction algorithm with respect to the prescribed mesostructural characteristics, 20 realizations were generated for each of the specified radial positions. The mean and standard deviation of the relative error for overall and type-specific characteristics compared to the target characteristics are summarized in Table 3. The results indicate that the algorithm successfully minimizes the overall fiber bundle area fraction as intended. However, this optimization leads to deviations in the prescribed area distribution of the vascular bundles, resulting in increased errors in both the average and standard deviation of the fiber bundle area. Furthermore, in configurations involving multiple vascular bundle types, the type-specific area fractions are notably impacted. This effect is also attributed to discretization artifacts arising from the finite number of vascular bundles, which in turn lead to quantifiable errors in the type-specific number densities. Nevertheless, given that a converged solution for the effective stiffness is achieved, it can be inferred that variations in the fiber bundle area distribution and type distribution exert only a minor influence on the effective stiffness, in comparison to the overall fiber bundle area fraction and the type-specific shape of the vascular bundles. These findings suggest that the employed algorithm is adequate for generating representative realizations of the bamboo mesostructure. However, the influence of the orientation distribution of vascular bundles could not be assessed due to limitations of the reconstruction algorithm, and it remains uncertain whether this characteristic has a significant impact on the effective mechanical properties.

3.3. Predictions of the homogenization models

According to Section 2.4, ergodic substitute models are considered at a finite number of normalized radial positions to predict the macroscopic stiffness distribution within the bamboo culm wall. These local substitute models reflect the modeled characteristics at the corresponding radial positions, as described in Section 3.1. Moreover, the substitute models comprise only the fiber bundles and the matrix material, which are modeled as linear elastic with mechanical properties given in Table 2. The hollow vessel system is not considered, as its characterization is not feasible with the applied imaging

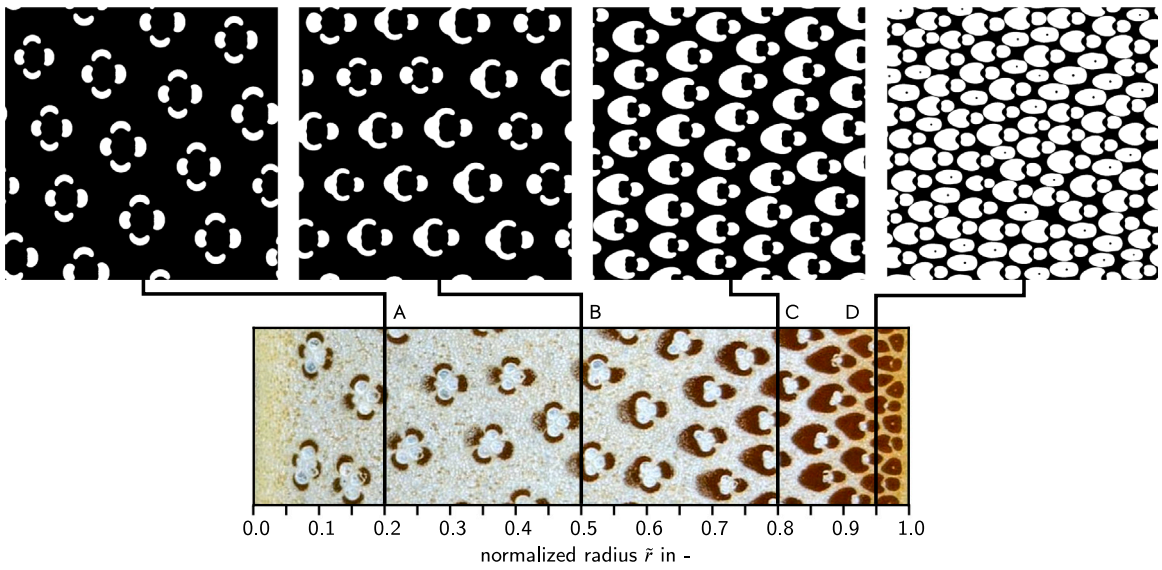

Fig. 10. Comparison between a realization of the bamboo mesostructure and four reconstructed representative images corresponding to the normalized radial positions $\tilde{r} = 0.2$, 0.5, 0.8, and 0.95.

Table 3
Relative error of the reconstructed characteristics compared to the target characteristics at different radial positions. Errors are expressed as the mean and standard deviation over 20 reconstructed realizations per position.

$\tilde{r}$	type	err($a^{\mathrm{fb},i}$) in %	err($\bar{A}^{\mathrm{fb},i}$) in %	err($\hat{A}^{\mathrm{fb},i}$) in %	err($n^{\mathrm{fb},i}$) in %
$\tilde{r}_A$	all	0.029 ± 0.012	0.029 ± 0.012	0.711 ± 0.500	0.000 ± 0.000
	VB1	0.029 ± 0.012	0.029 ± 0.012	0.711 ± 0.500	0.000 ± 0.000
	VB2	0.000 ± 0.000	0.000 ± 0.000	0.000 ± 0.000	0.000 ± 0.000
	VB3	0.000 ± 0.000	0.000 ± 0.000	0.000 ± 0.000	0.000 ± 0.000
$\tilde{r}_B$	all	0.020 ± 0.011	0.018 ± 0.009	0.935 ± 0.671	0.163 ± 0.000
	VB1	5.197 ± 0.108	0.414 ± 0.114	1.310 ± 0.857	5.588 ± 0.000
	VB2	2.795 ± 0.060	0.223 ± 0.058	0.648 ± 0.523	3.025 ± 0.000
	VB3	0.000 ± 0.000	0.000 ± 0.000	0.000 ± 0.000	0.000 ± 0.000
$\tilde{r}_C$	all	0.011 ± 0.005	0.011 ± 0.005	0.423 ± 0.279	0.000 ± 0.000
	VB1	0.000 ± 0.000	0.000 ± 0.000	0.000 ± 0.000	0.000 ± 0.000
	VB2	0.011 ± 0.005	0.011 ± 0.005	0.423 ± 0.279	0.000 ± 0.000
	VB3	0.000 ± 0.000	0.000 ± 0.000	0.000 ± 0.000	0.000 ± 0.000
$\tilde{r}_D$	all	0.042 ± 0.105	3.854 ± 0.101	5.792 ± 2.775	0.121 ± 0.000
	VB1	0.000 ± 0.000	0.000 ± 0.000	0.000 ± 0.000	0.000 ± 0.000
	VB2	0.236 ± 0.135	0.220 ± 0.183	5.660 ± 6.748	0.335 ± 0.000
	VB3	0.652 ± 0.345	0.448 ± 0.355	5.400 ± 8.497	0.909 ± 0.000

method described in Section 2.2 and therefore lies beyond the scope of this study. For the mean-field approach, only the fiber bundle volume fraction is considered, while the vascular bundles are represented as unidirectional, needle-shaped inclusions aligned with the longitudinal axis. Consequently, the substitute models are invariant along the longitudinal direction, and the volume fraction corresponds directly to the investigated fiber bundle area fraction. In the FFT-based modeling approach, representative mesostructural images, illustrated in Section 3.2, are employed as local substitute models. This enables the numerical method to incorporate detailed structural information, surpassing the level of abstraction found in mean-field approaches. Consequently, it enables more accurate predictions of macroscopic mechanical behavior compared to the mean-field models, establishing the numerical approach as benchmark model for this study. Still, experimental data needs to be considered to validate the predicted results of both mean-field and FFT-based models.

The predictions of all homogenization approaches for the macroscopic stiffness at normalized radial positions $\tilde{r}_A = 0.2$, $\tilde{r}_B = 0.5$, $\tilde{r}_C = 0.8$ and $\tilde{r}_D = 0.95$ are presented in Fig. 11. Following the methodology described in Böhlke and Brüggemann [73], the direction-dependent Young's moduli derived from the predicted stiffness tensors are plotted for varying orientations within the longitudinal–transversal cross-section. This representation enables the visualization of the anisotropy of the macroscopic stiffness. At all radial positions, the Voigt (V) and Reuss (R) models exhibit isotropic behavior and serve as physical upper and lower bounds for the macroscopic stiffness, respectively. All other homogenization models yield predictions that lie within these bounds. The Hashin–Shtrikman bounds ($\mathrm{HS}^{+/-}$) and the self-consistent (SC) model result in transversely isotropic stiffness tensors, which are invariant under rotations about the longitudinal axis. In contrast, the FFT-based model (FFT) predicts monoclinic symmetry, which arises from the circumferential symmetry of the vascular bundle distribution. Despite the monoclinic nature of the FFT predictions, the orthotropic error, defined by Eqs. (51), remains below 1% for all radial positions. This supports the approximation of the bamboo culm wall as an orthotropic material, consistent with findings from previous studies such as Al-Rukaibawi et al. [49]; Akinbade et al. [74]; Cui et al. [48]. To further illustrate the orthotropic characteristics of the FFT-based model, the direction-dependent Young's modulus is evaluated in both the longitudinal–circumferential (z, φ) and longitudinal–radial (z, r) cross-sections. For radial positions up to $\tilde{r} = 0.8$, no significant differences in modulus distribution are observed between the two planes, indicating a negligible transverse isotropy error. At higher radial positions, the differences become more pronounced but remain relatively small. Based on these findings, the authors suggest that the bamboo culm wall can be approximately modeled as a transversely isotropic material, which is sufficiently accurate for most engineering applications. The engineering constants derived from the macroscopic stiffness predictions of the homogenization models are presented in Fig. 12. Their distribution is plotted against the overall fiber bundle area fraction, which increases monotonically with the normalized radial position $\tilde{r}$ and can therefore be directly related to it. Since the mean-field models yield transversely isotropic stiffness tensors, the engineering constants are reported with respect to the longitudinal and transverse directions. The FFT-based solution exhibits only minor numerical artifacts, indicating stable convergence across all 50 investigated radial positions, including those corresponding to the minimum and maximum fiber bundle area fractions. Because the FFT-based model predicts an orthotropic stiffness, the engineering constants for the FFT-based model are plotted jointly for the radial and circumferential directions when considering the transverse axis. Fig. 12(a) illustrates that the predicted longitudinal Young's modulus increases

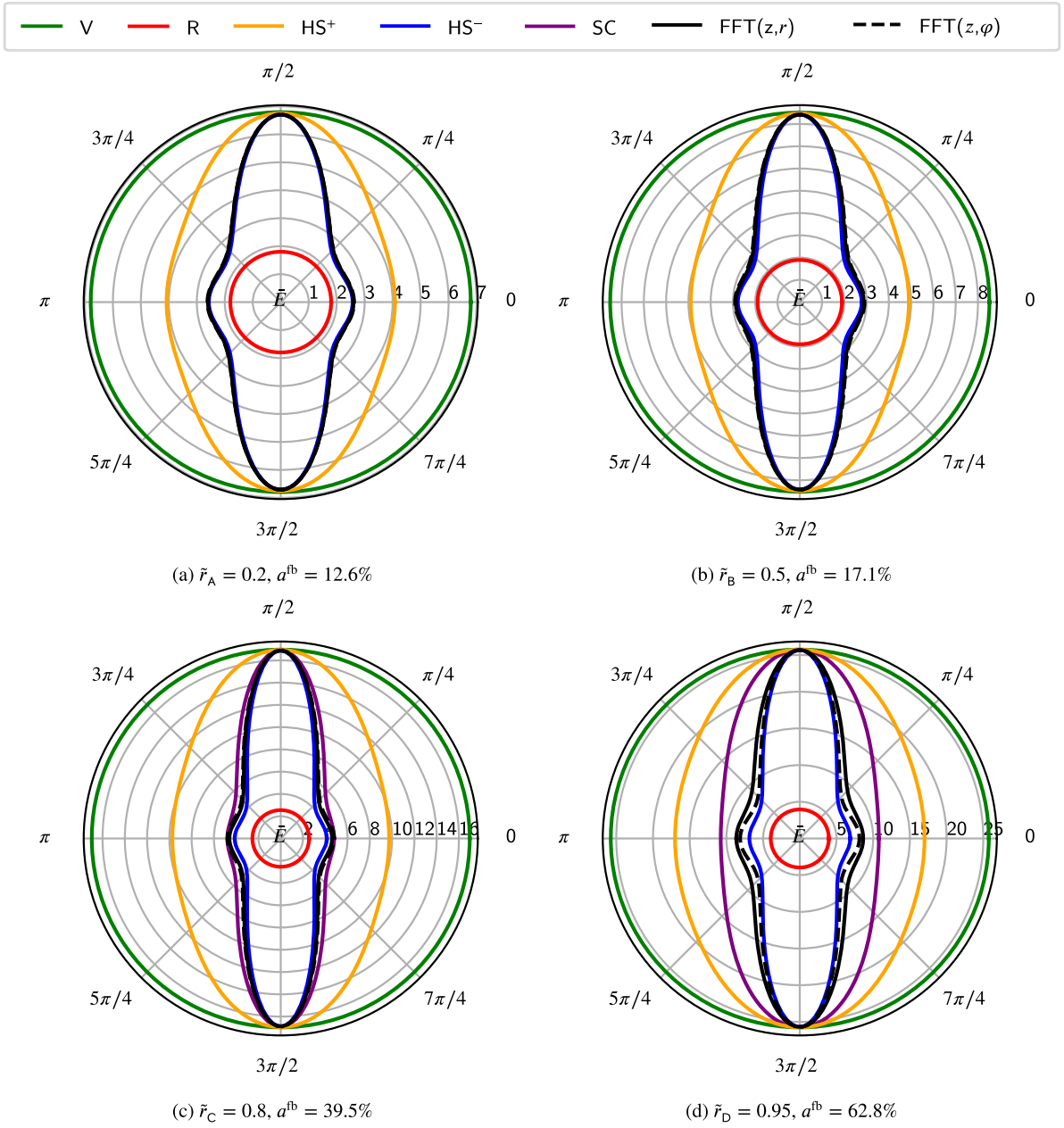

Fig. 11. Direction-dependent Young's modulus of the predicted macroscopic stiffness with respect to the longitudinal–transversal cross-section at four normalized radial positions. The solution of the FFT-based model is given in longitudinal–radial (z, r) and longitudinal–circumferential (z, φ) cross-section due to its orthotropic symmetry.

linearly with the fiber bundle area fraction for all models except the Reuss model. The values range from approximately 6 GPa to 30 GPa within the bounds corresponding to the intermediate layer, which aligns with the experimental results of Dixon and Gibson [8]. This linear behavior is characteristic of unidirectional long fiber-reinforced composites and is also reflected in Fig. 11. The distribution of the transverse Young's modulus, shown in Fig. 12(a), reveals that the FFT-based predictions for the radial and circumferential directions, as well as the self-consistent model, lie between the Hashin–Shtrikman bounds across all area fractions and corresponding radial positions. A similar trend is observed for the shear moduli in both the longitudinal–transverse directions and within the transverse plane, as illustrated in Fig. 12(b). The comparison of FFT-based predictions for the radial and circumferential directions reveals only minor differences, supporting the validity of the transverse isotropy assumption. The numerically predicted transverse Young's moduli range from approximately 2.5 GPa to 13 GPa. In contrast, semi-experimental data reported by Moran et al. [75] indicate circumferential Young's moduli between 1.1 GPa and 2.6 GPa. Other studies [76,77] on Moso bamboo's transverse properties report even lower values. Accessing the full anisotropy of the culm wall is experimentally challenging due to its inherent curvature, which results in lacking validation data and substantial model simplifications for the parameter identification in the named reference studies. The discrepancy between the predicted and experimentally derived values is likely due to the inherent anisotropy of the fiber bundles and matrix material, which is not explicitly represented in the current model, only accounting for morphological anisotropy as described in Section 2.4. Among the mean-field models, the lower Hashin–Shtrikman bound, which coincides with the Mori–Tanaka model in this case, shows the closest agreement with the FFT-based benchmark. Although the deviation between this mean-field model and the FFT-based predictions

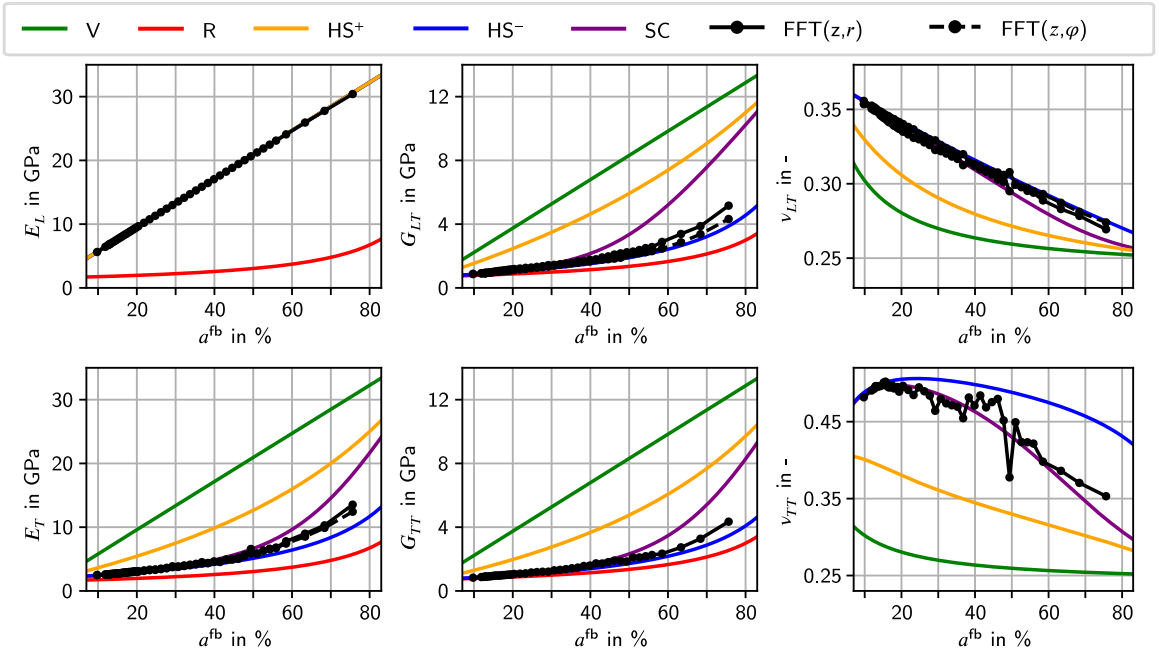

(a) Youngs Modulus (b) Shear Modulus (c) Poisson Ratio

Fig. 12. Engineering constants of the predicted macroscopic stiffness across fiber bundle are fraction. Due to its orthotropic symmetry, the FFT solution is given jointly for the radial and circumferential directions when considering the transverse axis.

increases with fiber bundle area fraction, it remains within an acceptable range. Given that the Hashin–Shtrikman lower bound represents a conservative estimate, its use is considered suitable for engineering applications.

4. Summary and conclusion

This study presents a comprehensive multiscale framework for analyzing the mesostructure of bamboo, addressing key limitations of existing approaches that often rely on averaged properties and simplified structural representations. In particular, the radial distribution of mesostructural characteristics and the resulting macroscopic linear elastic behavior of the bamboo culm wall are investigated and compared to results reported in literature. Based on the findings of this study, it can be concluded:

- Compared to previous studies, the proposed micromechanical framework comprising characterization, local reconstruction, and first-order homogenization enables more accurate and spatially resolved predictions of macroscopic mechanical properties incorporating detailed mesostructural information.
- A comprehensive set of first and second-order micromechanical descriptors for statistically inhomogeneous particle structures was successfully formulated, extending the indicator function concepts of Torquato [27]. This provides a robust basis for analyzing complex natural composites.
- The generalized framework was effectively applied to bamboo internode cross-sections using advanced image processing. Spatially resolved structural features were extracted, and differentiation between vascular bundle types enabled the quantification of multimodal distributions in morphology and arrangement. Direct representation of fiber bundle geometry from image data ensures high fidelity in structural characterization.
- An anatomy-based reconstruction algorithm was implemented to generate local mesostructural models that preserve prescribed characteristics. Through optimized tessellation and area fraction control, non-overlapping vascular bundle configurations were achieved. Resolution and representativity studies confirmed the capability to identify representative mesostructural images for any radial position, ensuring accurate macroscopic behavior.
- Classical mean-field and FFT-based numerical homogenization methods were successfully applied to the surrogate models, enabling computation of the radial distribution of macroscopic elastic properties across the culm wall. Results demonstrate low transverse-plane anisotropy, and the Hashin–Shtrikman lower bound was validated as both a theoretical limit and the closest mean-field approximation to FFT predictions.

The presented framework demonstrates the potential of integrating advanced micromechanical and numerical methods into the analysis of bamboo's mesostructure. By enabling spatially resolved predictions of macroscopic mechanical behavior, this approach contributes to a deeper understanding of structure–property relationships in natural fiber composites and lays the foundation for future bio-inspired or bamboo-based construction material.

CRediT authorship contribution statement

Lukas Speichinger: Writing – review & editing, Writing – original draft, Visualization, Software, Project administration, Methodology, Investigation, Formal analysis, Data curation, Conceptualization. **Ralf Förster:** Writing – review & editing, Supervision, Resources, Project administration. **Thomas Böhlke:** Writing – review & editing, Supervision, Resources, Project administration, Funding acquisition.

Funding sources

This research did not receive any specific grant from funding agencies in the public, commercial, or not-for-profit sectors.

Declaration of competing interest

The authors declare that they have no known competing financial interests or personal relationships that could have appeared to influence the work reported in this paper.

Appendix A. Nomenclature

General Characterization

ω	Realization
Ω	Ensemble
V_ω	Volume of a realization ω
α	Phase index
I^α_ω	Indicator function of phase α in realization ω
P	Particle index
$\mathcal{P}^\alpha_\omega$	Set of all particle indices of Phase α in realization ω
$I^\alpha_{\omega,P}$	Indicator function of particle P of phase α in realization ω
$\underline{z}^\alpha_{\omega,P}$	Set of morphological parameters of particle P of phase α in realization ω
$V^\alpha_{\omega,P}$	Volume of particle P of phase α in realization ω
$\boldsymbol{Q}^\alpha_{\omega,P}$	Orientation tensor of particle P of phase α in realization ω
$s^\alpha_{\omega,P}$	Shape of particle P of phase α in realization ω
$\underline{Z}^\alpha_{\omega,P}$	Parameter function of particle P of phase α in realization ω
$\underline{Z}^\alpha_\omega$	Parameter function of phase α in realization ω
$\langle\cdot\rangle$	Average over ensemble Ω
v^α	Volume fraction of phase α
Ω^α	Subset of ensemble Ω with phase α at position $\boldsymbol{x}$
$\langle\cdot\rangle_\alpha$	Average over ensemble Ω^α
$\underline{\mu}^\alpha$	Average of morphological parameters of phase α
$\underline{k}^\alpha$	Covariances of morphological parameters of phase α
n^α	Particle number density of phase α

Bamboo Characterization

L_{IN}	Internode Length
D_{IN}	Outer diameter of an internode
δ_{IN}	Internode wall thickness
VB	Vascular bundle index
$A^{\mathrm{fb}}_{\omega,\mathrm{VB}}$	Cross-sectional fiber bundle area of a vascular bundle
$\varphi^{\mathrm{fb}}_{\omega,\mathrm{VB}}$	Vascular bundle orientation angle
$s^{\mathrm{fb}}_{\omega,\mathrm{VB}}$	Cross sectional fiber bundle shape of a vascular bundle
$\boldsymbol{J}^{\mathrm{fb}}_{\omega,\mathrm{VB}}$	Second-order area moment of vascular bundle cross section
$h^{\mathrm{fb}}_{\omega,\mathrm{VB}}$	Height of bounding box
$w^{\mathrm{fb}}_{\omega,\mathrm{VB}}$	Width of bounding box
$\alpha^{\mathrm{fb}}_{\omega,\mathrm{VB}}$	Aspect ratio of bounding box
$\tilde{r}$	Normalized radial position
$a^{\mathrm{fb},i}$	Type-specific fiber bundle volume fraction
$\underline{\mu}^{\mathrm{fb},i}$	Type-specific average vascular bundle morphology
$\underline{\sigma}^{\mathrm{fb},i}$	Type-specific standard deviation of vascular bundle morphology
$n^{\mathrm{fb},i}$	Type-specific number density
$D^{\mathrm{fb}}_{\omega,\mathrm{VB}}$	Domain area of a vascular bundle

Micromechanics

$\mathbb{C}$	Stiffness tensor
$\boldsymbol{\varepsilon}$	Strain tensor
$\boldsymbol{\sigma}$	Cauchy stress tensor
$\mathbb{A}$	Strain localization tensor
$\mathbb{P}_0$	Hill's polarizations tensor
V	Voigt bound
R	Reuss bound
HS-	Hashin–Shtrikmann lower bound
HS+	Hashin–Shtrikmann upper bound
SC	Self-consistent method
FFT	Fast Fourier Transform

Appendix B. Training and evaluation of Weka and YOLO models

The Weka segmentation model is trained based on two radially oriented, cross-sectional image stripes from each internode. Therefore matrix and fiber phases are labeled manually, and the Weka classifier is refined incrementally until the overlay of the predicted segmentation with the original image attains an acceptable level of visual accuracy. Quantitative metrics for evaluating the model precision cannot be derived, as no objective reference data are available. Notably, segmentation errors affect the measurement of the mesostructural characteristics and therefore need to be monitored after model application.

The YOLO model for vascular bundle detection is trained on a subset comprising 70% of annotated image stripes. This dataset is obtained by manually grouping and classifying fiber bundles in 62 images collected during the preliminary phase of the study, which employed the same bamboo specimens as in the subsequent analysis. The remaining data is split into a validation set and an independent test set consisting of 20% and 10% of the annotated images, respectively. Evaluation on the test set, summarized in Table B.4, yield a mean and type-specific average precision (AP_{50}) of 99% regarding an intersection-over-union (IoU) threshold of 50%. The same level of performance is observed for the corresponding precision (P) and recall (R) metrics. Typically, for densely packed object-detection scenarios, e.g., the outer culm-wall region, the mean and type-specific $AP_{50:95}$ scores are about 10%–20% lower than the corresponding AP_{50} values, reflecting the stronger penalization of localization errors at higher IoU thresholds [78]. The few detection errors that occur arise from confusion between vascular bundle types or from false negatives and consequently have a negligible influence on the statistical distribution of the morphological parameters.

Table B.4
Performance metrics of the YOLO-based model for vascular bundle detection regarding an independent test set of 6 images.

metric	all	VB1	VB2	VB3
Instances	348	84	200	64
P	0.989	0.988	0.995	0.985
R	0.997	1.000	0.990	1.000
AP_{50}	0.990	0.989	0.990	0.990
$AP_{50:95}$	0.878	0.927	0.902	0.807

Appendix C. Morphological parameters of a particle

The particle volume $V^\alpha_{\omega,P}$ is defined as the zeroth-order volume moment and is obtained from the particle indicator function according to

$$V^\alpha_{\omega,P} = \int_{V_\omega} I^\alpha_{\omega,P}(\boldsymbol{x})\,\mathrm{d}V. \tag{36}$$

The volumetric centroid of the particle is given by the first-order volume moment,

$$\boldsymbol{x}^\alpha_{\omega,P} = \int_{V_\omega} I^\alpha_{\omega,P}(\boldsymbol{x})\,\boldsymbol{x}\,\mathrm{d}V, \tag{37}$$

while the second-order volume moment, denoted by $\boldsymbol{J}^\alpha_{\omega,P}$, is defined as

$$\boldsymbol{J}^\alpha_{\omega,P} = \int_{V_\omega} I^\alpha_{\omega,P}(\boldsymbol{x})\,[(\boldsymbol{x}\cdot\boldsymbol{x})\,\boldsymbol{I} - \boldsymbol{x}\otimes\boldsymbol{x}]\,\mathrm{d}V. \tag{38}$$

The particle orientation $\boldsymbol{Q}^{\alpha}_{\omega,P}$ is determined from the principal directions of $\boldsymbol{J}^{\alpha}_{\omega,P}$, obtained by solving the eigenvalue problem

$$\det \boldsymbol{J}^{\alpha}_{\omega,P} - \lambda_i \boldsymbol{I} = 0, \qquad \left(\boldsymbol{J}^{\alpha}_{\omega,P} - \lambda_i \boldsymbol{I}\right)\mathbf{v}_i = \mathbf{0}, \tag{39}$$

where λ_i and $\mathbf{v}_i$ denote the eigenvalues and corresponding eigenvectors of $\boldsymbol{J}^{\alpha}_{\omega,P}$. The particle orientation tensor is then given by

$$\boldsymbol{Q}^{\alpha}_{\omega,P} = \mathbf{v}_i \otimes \mathbf{e}_i. \tag{40}$$

In the two-dimensional case restricted to the x-y plane, the second-order area moments of a particle are given by

$$\begin{aligned} J^{\alpha}_{\omega,P,xx} &= \sum^{\alpha}\sum_{n} I^{\alpha}_{\omega,P}[m,n](n+1/2)^2 h^4, \\ J^{\alpha}_{\omega,P,yy} &= \sum^{\alpha}\sum_{n} I^{\alpha}_{\omega,P}[m,n](m+1/2)^2 h^4, \\ J^{\alpha}_{\omega,P,xy} &= \sum^{\alpha}\sum_{n} I^{\alpha}_{\omega,P}[m,n](n+1/2)(m+1/2) h^4, \end{aligned} \tag{41}$$

where $I^{\alpha}_{\omega,P}[m,n]$ denotes the discrete particle indicator function represented as a binary image with pixel edge length h. In this two-dimensional setting, the eigenvalue problem reduces to a single particle orientation angle $\varphi^{\alpha}_{\omega,P}$ given by

$$\tan(2\varphi^{\alpha}_{\omega,P}) = \frac{2J^{\alpha}_{\omega,P,xy}}{J^{\alpha}_{\omega,P,xx} - J^{\alpha}_{\omega,P,yy}}. \tag{42}$$

Appendix D. Hill's polarization tensor

For an ellipsoidal shaped inclusion defined by a tensor $\boldsymbol{A}\hat{=}\mathrm{diag}(a_1^{-1}, a_2^{-1}, a_3^{-1})$ and an elliptical equation $||\boldsymbol{A}\boldsymbol{x}|| = 1$, Hill's Polarization tensor is given by Willis [63] as

$$\mathbb{P}_0 = \frac{1}{4\pi \det \boldsymbol{A}} \int_{\partial S} \frac{\mathbb{H}(\mathbb{C}_0, \boldsymbol{n})}{||\boldsymbol{A}^{-1}\boldsymbol{n}||^3}\, \mathrm{d}S \tag{43}$$

$$\mathbb{H} = \mathbb{I}^{\mathrm{S}}(\boldsymbol{K}^{-1}\square(\boldsymbol{n}\otimes\boldsymbol{n}))\mathbb{I}^{\mathrm{S}}, \quad \boldsymbol{K}\hat{=}C_{0,ikjl}n_k n_l \tag{44}$$

with $S = \left\{\boldsymbol{n}\in\mathbb{R}^3 : ||\boldsymbol{n}|| = 1\right\}$. In the Notation of Walpole [79], a transversely isotropic tensor $\mathbb{C}$ with a symmetry axis in x_3-direction is represented by

$$\mathbb{C}\hat{=}(2k, l, n, 2m, 2p), \tag{45}$$

which translates in normalized Voigt notation to

$$\mathbb{C}\hat{=}\begin{pmatrix} k+m & k-m & l & & & \\ k-m & k+m & l & & & \\ l & l & n & & & \\ & & & 2p & & \\ & & & & 2p & \\ & & & & & 2m \end{pmatrix}. \tag{46}$$

Considering a transversal isotropic reference stiffness $\mathbb{C}_0 = (2k_0, l_0, n_0, 2m_0, 2p_0)$, the elastic constants in Walpole's notation can be given in relation to the engineering constants by

$$k_0 = \left(\frac{2(1-\nu_{TT})}{E_T} - \frac{4\nu_{LT}^2}{E_L}\right)^{-1}, \quad l = 2k_0\nu_{LT}, \tag{47}$$

$$n = E_L + \frac{l^2}{k}, \quad m = G_{TT}, \quad p = G_{LT}, \tag{48}$$

where L and T denote the direction parallel and transversal to the symmetry axis, respectively. For a needle shaped inclusion and transversely isotropic reference material with the same orientation, Walpole [79] derives the Hill's polarization to

$$\mathbb{P}_0\hat{=}\left(\frac{1}{2\left(k_0+m_0\right)}, 0, 0, \frac{k_0+2m_0}{4(k_0+m_0)m_0}, \frac{1}{4p_0}\right). \tag{49}$$

If the reference material is fully isotropic, Hill's Polarization tensor reduces to

$$\mathbb{P}_0\hat{=}\left(\frac{1}{2\left(\lambda_0+2\mu_0\right)}, 0, 0, \frac{\lambda_0+3\mu_0}{4(\lambda_0+2\mu_0)\mu_0}, \frac{1}{4\mu_0}\right), \tag{50}$$

where λ_0 and μ_0 are the Lamé constants of the isotropic reference material. In the Self Consistent model, the transversely isotropic effective stiffness works as reference material and the polarization tensor is calculated by Eq. (49). In the Mori Tanaka model the isotropic matrix material is the reference material, so Eq. (50) is used for the polarization tensor.

Appendix E. Numerical studies

E.1. Resolution study

Accurate computation of the effective stiffness tensor requires sufficiently fine spatial resolution. However, decreasing pixel size increases the computational cost of the FFT-based homogenization. To balance accuracy and efficiency, a resolution study is conducted using quadratic cell with an edge length $Q = 3\mathrm{mm}$. To evaluate the resolution for different local surrogate models of the mesostructure, four characteristic normalized radial positions $\tilde{r}_{\mathrm{A}} = 0.2$, $\tilde{r}_{\mathrm{B}} = 0.5$, $\tilde{r}_{\mathrm{C}} = 0.8$ and $\tilde{r}_{\mathrm{D}} = 0.95$ are considered. Fig. 7(c) shows the local models of the mesostructure for these given radial positions. Pixel-edge lengths $h = 8\ \mu\mathrm{m}, 4\ \mu\mathrm{m}, 2\ \mu\mathrm{m}$ and $1\ \mu\mathrm{m}$ are analyzed. The total pixel count ranges from $375^2 \approx 14\times10^4$ (coarsest) to $3000^2 = 9\times10^6$ (finest), significantly affecting computational runtime. Representative microstructures for $\tilde{r} = 0.5$ at the coarsest and finest resolutions are shown in Figs. 13(a)

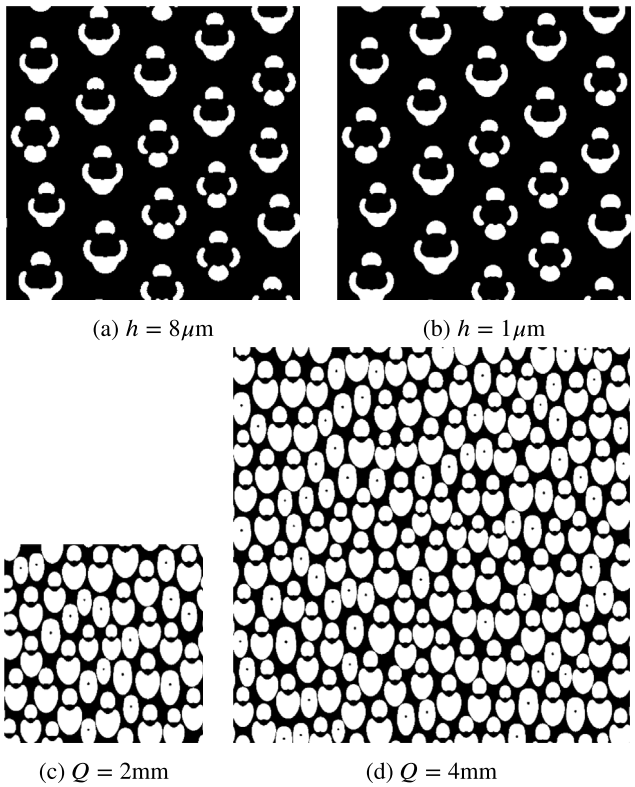

(a) $h = 8\mu\mathrm{m}$ (b) $h = 1\mu\mathrm{m}$

(c) $Q = 2\mathrm{mm}$ (d) $Q = 4\mathrm{mm}$

Fig. 13. Local models of the mesostructure at radial position $\tilde{r}_{\mathrm{B}} = 0.5$ with a cell-edge length of $Q = 3\mathrm{mm}$ and different pixel-edge lengths (a,b) for resolution study. Local models at radial position $\tilde{r} = 0.95$ with different cell-edge lengths (c,d) and a pixel-edge length of $h = 2\ \mu\mathrm{m}$ for representativity study.

Table E.5
Engineering constants of the orthotropic approximation for pixel-edge lengths $h = 8$ µm, 4 µm, 2 µm and 1 µm.

$\tilde{r}$ –	h µm	E_r GPa	E_φ GPa	E_z GPa	$G_{\varphi z}$ GPa	G_{rz} GPa	$G_{r\varphi}$ GPa	e_{orth} %
$\tilde{r}_A$	8	2.60	2.62	6.70	0.93	0.93	0.89	0.09
	4	2.60	2.62	6.71	0.93	0.93	0.89	0.05
	2	2.60	2.62	6.71	0.93	0.93	0.89	0.04
	1	2.60	2.62	6.71	0.93	0.92	0.89	0.03
$\tilde{r}_B$	8	2.87	2.90	8.40	1.08	1.05	0.98	0.17
	4	2.87	2.90	8.40	1.07	1.05	0.98	0.14
	2	2.87	2.91	8.42	1.07	1.05	0.98	0.13
	1	2.87	2.91	8.43	1.07	1.05	0.98	0.12
$\tilde{r}_C$	8	4.57	4.76	16.76	1.74	1.69	1.53	0.19
	4	4.58	4.77	16.82	1.74	1.68	1.53	0.14
	2	4.59	4.79	16.86	1.74	1.68	1.52	0.14
	1	4.60	4.80	16.90	1.74	1.68	1.52	0.14
$\tilde{r}_D$	8	8.42	8.31	25.49	2.94	3.25	2.80	0.60
	4	8.41	8.36	25.60	2.90	3.20	2.76	0.28
	2	8.38	8.36	25.63	2.87	3.17	2.74	0.18
	1	8.40	8.40	25.69	2.88	3.16	2.74	0.16

Table E.6
Fitted model parameters for fiber bundle area fraction of VB1, VB2, and VB3.

	VB1	VB2	VB3
a_1	−0.69413	0.78424	72.376
b_1	0.37911	−0.07372	−124.29
c_1	0.07812	−0.04794	52.922
a_2	−0.58792	−66.121	−3459.8
b_2	0.12583	116.63	6754.9
c_2	0.14429	−50.669	−3296.5
x_1	0.24225	0.29868	0.93619
x_2	0.29868	0.93619	0.97933
x_3	0.61384	0.98951	0.98995

Table E.7
Fitted model parameters for fiber bundle area of vascular bundles VB1, VB2, and VB3.

	VB1	VB2	VB3
a	−2.0195	−1.9557	−882.77
b	3.1915	4.3479	3366.4
c	−1.9264	−3.4994	−4809.3
d	0.51365	1.2342	3050.2
e	0.02592	−0.08318	−724.47
x_1	0.05643	0.29868	0.93619
x_2	0.61384	0.98951	0.98995

and 13(b), respectively. Results are summarized in Table E.5 showing the engineering constants of the orthotropic approximation $\mathbb{C}_{orth}$ of the computed stiffness $\mathbb{C}$ and the approximation error

$$err_{orth} = \frac{||\mathbb{C} - \mathbb{C}_{orth}||}{||\mathbb{C}||}. \quad (51)$$

The required resolution is determined by comparing the elastic properties of coarser meshes to those of the finest mesh. The coarsest resolution yielding a relative deviation below 1% is selected. A pixel-edge length of $h = 2$ µm satisfies this criterion for all radial positions and is adopted for subsequent analyses.

E.2. Representativity study

In computational homogenization, material properties are evaluated using unit cells. Representativity refers to the ability of a unit cell to approximate the effective macroscopic properties, which emerge deterministically as the unit cell volume approaches infinity [80–82]. For finite-sized unit cells, the computed apparent properties exhibit randomness due to microstructural variability. As unit cell size increases, these properties converge almost surely to the effective values, reducing variability. A representative volume element (RVE) is defined as the smallest unit cell for which the apparent properties approximate the effective properties with sufficient accuracy. To minimize computational cost, the smallest possible RVE should be employed. Representativity can be assessed statistically by analyzing both random and systematic errors [80,83]. The random error (dispersion) quantifies the variance across multiple realizations of a fixed unit cell size and vanishes with increasing size. The systematic error (bias) measures the deviation between the mean apparent properties and the effective properties. Since the latter are typically unknown, convergence of the mean values across increasing unit cell sizes is used as a proxy. To study the representativity, quadratic unit cells are generated with cell-edge length of Q = 2mm, 3mm and 4mm resolved with pixel-edge length $h = 2$ µm as result of the resolution study. Hence, the total pixel count ranges from 1000^2 for the smallest cell to 2000^2 for the biggest cell. Exemplary realizations for $\tilde{r} = 0.95$ are shown in Figs. 13(c) and 13(d). For each unit cell size, ten realizations are generated. The average and standard deviation of the orthotropic engineering constants are reported in Table E.8. In all cases, the orthotropic approximation error remains below 1%, indicating that the effective elastic behavior can be considered orthotropic. For a cell-edge length of Q = 3mm the systematic error compared to the biggest cell is a maximum of 1% and the coefficient of variance is smaller than 2%. Thus, this cell size may be considered sufficiently representative for further investigation of the stiffness distribution trough the bamboo culm wall.

Appendix F. Models of structural characteristics

The radial distributions of the type-specific fiber bundle area fractions is modeled by a piecewise quadratic function

$$f(x) = \begin{cases} 0 & ,x \in [0, x_1) \\ a_1x^2 + b_1x + c_1 & ,x \in [x_1, x_2) \\ a_2x^2 + b_2x + c_2 & ,x \in [x_2, x_3) \\ 0 & ,x \in [x_3, 1] \end{cases}. \quad (52)$$

The parameters a_1, b_1, c_1, a_2, b_2, c_2, x_1, x_2 and x_3 are derived by fitting the model to measured data with a least-square method and are presented in Table E.6. The radial distributions of the type-specific fiber bundle area of a vascular bundle is modeled by a piecewise fourth-order polynomial function

$$f(x) = \begin{cases} 0 & ,x \in [0, x_1) \\ ax^4 + bx^3 + cx^2 + dx + e & ,x \in [x_1, x_2) \\ 0 & ,x \in [x_2, 1] \end{cases}. \quad (53)$$

The fitted model parameters a, b, c, d, e, x_1 and x_2 are listed in Table E.7.

Data availability

The dataset employed for development of the YOLO-based vascular bundle detection model is publicly available from Speichinger et al. [84]. The dataset used for mesostructure characterization can be accessed via Speichinger et al. [85]. The source code implementing the image-processing workflow for mesostructure characterization is not publicly available but is provided by the corresponding author upon a reasonable request.

Table E.8
Engineering constants of the orthotropic approximation for cell-edge lengths Q = 2mm, 3mm and 4mm.

$\tilde{r}$ –	Q mm	E_r GPa	E_φ GPa	E_z GPa	$G_{\varphi z}$ GPa	G_{rz} GPa	$G_{r\varphi}$ GPa	e_{orth} %
$\tilde{r}_A$	2	2.59 ± 0.02	2.61 ± 0.01	6.71 ± 0.00	0.93 ± 0.00	0.93 ± 0.00	0.89 ± 0.01	0.03
	3	2.60 ± 0.01	2.62 ± 0.00	6.71 ± 0.00	0.93 ± 0.00	0.92 ± 0.00	0.89 ± 0.00	0.03
	4	2.60 ± 0.00	2.62 ± 0.00	6.71 ± 0.00	0.93 ± 0.00	0.93 ± 0.00	0.89 ± 0.00	0.04
$\tilde{r}_B$	2	2.87 ± 0.02	2.90 ± 0.01	8.43 ± 0.00	1.08 ± 0.00	1.05 ± 0.00	0.98 ± 0.01	0.08
	3	2.87 ± 0.02	2.91 ± 0.01	8.43 ± 0.00	1.08 ± 0.00	1.05 ± 0.00	0.98 ± 0.01	0.07
	4	2.85 ± 0.00	2.89 ± 0.01	8.43 ± 0.00	1.08 ± 0.00	1.05 ± 0.00	0.99 ± 0.00	0.05
$\tilde{r}_C$	2	4.44 ± 0.08	4.37 ± 0.20	16.90 ± 0.00	1.63 ± 0.05	1.76 ± 0.04	1.62 ± 0.04	0.22
	3	4.55 ± 0.03	4.57 ± 0.01	16.90 ± 0.00	1.67 ± 0.01	1.74 ± 0.02	1.58 ± 0.00	0.26
	4	4.53 ± 0.01	4.52 ± 0.05	16.90 ± 0.00	1.66 ± 0.03	1.74 ± 0.02	1.59 ± 0.00	0.17
$\tilde{r}_D$	2	8.57 ± 0.17	8.26 ± 0.06	25.69 ± 0.02	2.81 ± 0.02	3.25 ± 0.06	2.72 ± 0.01	0.35
	3	8.64 ± 0.10	8.34 ± 0.01	25.69 ± 0.02	2.83 ± 0.01	3.25 ± 0.06	2.72 ± 0.01	0.22
	4	8.59 ± 0.15	8.37 ± 0.05	25.71 ± 0.00	2.86 ± 0.04	3.24 ± 0.07	2.73 ± 0.01	0.32

References

[1] Y. Okahisa, K. Kojiro, H. Ashiya, T. Tomita, Y. Furuta, M. Yamamura, T. Umezawa, Age-dependent and radial sectional differences in the dynamic viscoelastic properties of bamboo culms and their possible relationship with the lignin structures, J. Wood Sci. 66 (2020) 1–9, http://dx.doi.org/10.1186/S10086-020-01914-Y, 2020 66:1.

[2] M. Chen, L. Guo, M. Ramakrishnan, Z. Fei, K.K. Vinod, Y. Ding, C. Jiao, Z. Gao, R. Zha, C. Wang, Z. Gao, F. Yu, G. Ren, Q. Wei, Rapid growth of moso bamboo (phyllostachys edulis): Cellular roadmaps, transcriptome dynamics, and environmental factors, Plant Cell 34 (2022) 3577–3610, http://dx.doi.org/10.1093/PLCELL/KOAC193.

[3] L. Binfield, T.L. Britton, C. Dai, J.L. Innes, Evidence on the social, economic, and environmental impact of interventions that facilitate bamboo industry development for sustainable livelihoods: A systematic map, Forests 16 (2025) 713, http://dx.doi.org/10.3390/F16050713/S1.

[4] D.L. Zariatin, J.K. Sibarani, D. Dahlan, R. Förster, Z. Adriant, Potential of Bamboo as Car Roof Material, J. Asiimetrik: J. Ilm. Rekayasa Dan Inov. (2022) 257–264, http://dx.doi.org/10.35814/asiimetrik.v4i1.3644.

[5] N.S. Kathiravan, R. Manojkumar, P. Jayakumar, J. Kumaraguru, V. Jayanthi, State of art of review on bamboo reinforced concrete, Mater. Today: Proc. 45 (2021) 1063–1066, http://dx.doi.org/10.1016/j.matpr.2020.03.159.

[6] A. Loth, R. Förster, Usage of a BAMBOO HONEYCOMB structure (COMBOO) in timber architecture, in: World Conference on Timber Engineering (WCTE 2023), World Conference on Timber Engineering (WCTE 2023), Oslo, Norway, 2023, pp. 3694–3700, http://dx.doi.org/10.52202/069179-0480.

[7] B. Fei, Economic value and research significance of moso bamboo, in: J. Gao (Ed.), The Moso Bamboo Genome, Springer International Publishing, Cham, 2021, pp. 1–12, http://dx.doi.org/10.1007/978-3-030-80836-5_1.

[8] P.G. Dixon, L.J. Gibson, The structure and mechanics of Moso bamboo material, J. R. Soc. Interface 11 (99) (2014) 20140321, http://dx.doi.org/10.1098/rsif.2014.0321.

[9] W. Liese, The Anatomy of Bamboo Culms, BRILL, 1998.

[10] N. Parameswaran, W. Liese, On the fine structure of bamboo fibres, Wood Sci. Technol. 10 (4) (1976) 231–246, http://dx.doi.org/10.1007/BF00350830.

[11] K. Hu, Y. Huang, B. Fei, C. Yao, C. Zhao, Investigation of the multilayered structure and microfibril angle of different types of bamboo cell walls at the micro/nano level using a LC-PolScope imaging system, Cellulose 24 (11) (2017) 4611–4625, http://dx.doi.org/10.1007/s10570-017-1447-y.

[12] F.L. Palombini, E.L. Lautert, J.E.D.A. Mariath, B.F. De Oliveira, Combining numerical models and discretizing methods in the analysis of bamboo parenchyma using finite element analysis based on X-ray microtomography, Wood Sci. Technol. 54 (1) (2020) 161–186, http://dx.doi.org/10.1007/s00226-019-01146-4.

[13] X. Chen, X. Wang, L. Shang, X. Ma, C. Fang, B. Fei, H. Liu, S. Zhang, Three-dimensional structural characterization and mechanical properties of bamboo parenchyma tissue, Ind. Crop. Prod. 208 (2024) 117833, http://dx.doi.org/10.1016/J.INDCROP.2023.117833.

[14] F. Nogata, H. Takahashi, Intelligent functionally graded material: Bamboo, Compos. Eng. 5 (7) (1995) 743–751, http://dx.doi.org/10.1016/0961-9526(95)00037-N.

[15] S. Amada, Y. Ichikawa, T. Munekata, Y. Nagase, H. Shimizu, Fiber texture and mechanical graded structure of bamboo, Compos. Part B: Eng. 28 (1–2) (1997) 13–20, http://dx.doi.org/10.1016/S1359-8368(96)00020-0.

[16] Z.P. Shao, C.H. Fang, S.X. Huang, G.L. Tian, Tensile properties of Moso bamboo (Phyllostachys pubescens) and its components with respect to its fiber-reinforced composite structure, Wood Sci. Technol. 44 (4) (2010) 655–666, http://dx.doi.org/10.1007/s00226-009-0290-1.

[17] H. Li, S. Shen, The mechanical properties of bamboo and vascular bundles, J. Mater. Res. 26 (21) (2011) 2749–2756, http://dx.doi.org/10.1557/jmr.2011.314.

[18] H. Liu, Z. Jiang, X. Zhang, X. Liu, Z. Sun, Effect of Fiber on Tensile Properties of Moso Bamboo, BioResources 9 (4) (2014) 6888–6898, http://dx.doi.org/10.15376/biores.9.4.6888-6898.

[19] L. Shang, Z. Sun, X. Liu, Z. Jiang, A novel method for measuring mechanical properties of vascular bundles in moso bamboo, J. Wood Sci. 61 (6) (2015) 562–568, http://dx.doi.org/10.1007/s10086-015-1510-y.

[20] L. Osorio, E. Trujillo, F. Lens, J. Ivens, I. Verpoest, A. Van Vuure, In-depth study of the microstructure of bamboo fibres and their relation to the mechanical properties, J. Reinf. Plast. Compos. 37 (17) (2018) 1099–1113, http://dx.doi.org/10.1177/0731684418783055.

[21] J. Li, H. Xu, Y. Yu, H. Chen, W. Yi, H. Wang, Intelligent analysis technology of bamboo structure. Part I: The variability of vascular bundles and fiber sheath area, Ind. Crop. Prod. 174 (2021) 114163, http://dx.doi.org/10.1016/J.INDCROP.2021.114163.

[22] J. Redmon, S. Divvala, R. Girshick, A. Farhadi, You only look once: Unified, real-time object detection, in: Proceedings of the IEEE Conference on Computer Vision and Pattern Recognition, 2016, pp. 779–788.

[23] H. Xu, J. Li, X. Ma, W. Yi, H. Wang, Intelligent analysis technology of bamboo structure. Part II: The variability of radial distribution of fiber volume fraction, Ind. Crop. Prod. 174 (2021) 114164, http://dx.doi.org/10.1016/J.INDCROP.2021.114164.

[24] H. Xu, Y. Zhang, J. Wang, J. Li, T. Zhong, X. Ma, H. Wang, A universal transfer-learning-based detection model for characterizing vascular bundles in phyllostachys, Ind. Crop. Prod. 180 (2022) http://dx.doi.org/10.1016/j.indcrop.2022.114705.

[25] T. Tsuyama, K. Hamai, Y. Kijidani, J. Sugiyama, Quantitative morphological transformation of vascular bundles in the culm of moso bamboo (phyllostachys pubescens), PLoS ONE 18 (2023) http://dx.doi.org/10.1371/journal.pone.0290732.

[26] J. Quintanilla, S. Torquato, Microstructure functions for a model of statistically inhomogeneous random media, Phys. Rev. E 55 (1997) 1558, http://dx.doi.org/10.1103/PhysRevE.55.1558.

[27] S. Torquato, Random Heterogeneous Materials: Microstructure and Macroscopic Properties, vol. 16, Springer, 2002, pp. 21–58.

[28] A.L. Kalamkarov, I.V. Andrianov, V.V. Danishevs'kyy, Asymptotic Homogenization of Composite Materials and Structures, Appl. Mech. Rev. 62 (030802) (2009) http://dx.doi.org/10.1115/1.3090830.

[29] M. Ostoja-Starzewski, Microstructural Randomness Versus Representative Volume Element in Thermomechanics, J. Appl. Mech. 69 (1) (2001) 25–35, http://dx.doi.org/10.1115/1.1410366.

[30] A. Bourgeat, A. Piatnitski, Approximations of effective coefficients in stochastic homogenization, Ann. L'Institut Henri Poincare (B) Probab. Stat. 40 (2) (2004) 153–165, http://dx.doi.org/10.1016/j.anihpb.2003.07.003.

[31] Y.S. Jetti, M. Ostoja-Starzewski, Correlation structures of statistically isotropic stiffness and compliance TRFs through upscaling, Comput. Methods Appl. Mech. Engrg. 432 (2024) 117356, http://dx.doi.org/10.1016/j.cma.2024.117356.

[32] D. Savvas, G. Stefanou, M. Papadrakakis, Determination of RVE size for random composites with local volume fraction variation, Comput. Methods Appl. Mech. Engrg. 305 (2016) 340–358, http://dx.doi.org/10.1016/j.cma.2016.03.002.

[33] T. Mori, K. Tanaka, Average stress in matrix and average elastic energy of materials with misfitting inclusions, Acta Metall. 21 (5) (1973) 571–574, http://dx.doi.org/10.1016/0001-6160(73)90064-3.

[34] Z. Hashin, S. Shtrikman, A variational approach to the theory of the elastic behaviour of multiphase materials, J. Mech. Phys. Solids 11 (1963) 127–140, http://dx.doi.org/10.1016/0022-5096(63)90060-7.

[35] J. Kochmann, L. Ehle, S. Wulfinghoff, J. Mayer, B. Svendsen, S. Reese, Efficient multiscale FE-FFT-based modeling and simulation of macroscopic deformation processes with non-linear heterogeneous microstructures, Lect. Notes Appl. Comput. Mech. 86 (2018) 129–146, http://dx.doi.org/10.1007/978-3-319-65463-8_7/FIGURES/6.

[36] K.A. Kalina, L. Linden, J. Brummund, M. Kästner, FE^{ANN}: an efficient data-driven multiscale approach based on physics-constrained neural networks and automated data mining, Comput. Mech. 71 (5) (2023) 827–851, http://dx.doi.org/10.1007/s00466-022-02260-0.

[37] X. Chao, W. Tian, F. Xu, D. Shou, A fractal model of effective mechanical properties of porous composites, Compos. Sci. Technol. 213 (2021) 108957, http://dx.doi.org/10.1016/j.compscitech.2021.108957.

[38] R. Ma, T.J. Truster, FFT-based homogenization of hypoelastic plasticity at finite strains, Comput. Methods Appl. Mech. Engrg. 349 (2019) 499–521, http://dx.doi.org/10.1016/j.cma.2019.02.037.

[39] M. Schneider, A review of nonlinear FFT-based computational homogenization methods, Acta Mech. 232 (6) (2021) 2051–2100, http://dx.doi.org/10.1007/s00707-021-02962-1.

[40] J. Kuhn, M. Schneider, P. Sonnweber-Ribic, T. Böhlke, Fast methods for computing centroidal laguerre tessellations for prescribed volume fractions with applications to microstructure generation of polycrystalline materials, Comput. Methods Appl. Mech. Engrg. 369 (2020) http://dx.doi.org/10.1016/j.cma.2020.113175.

[41] Y. Su, Z. Shen, X. Long, C. Chen, L. Qi, X. Chao, Gaussian filtering method of evaluating the elastic/elasto-plastic properties of sintered nanocomposites with quasi-continuous volume distribution, Mater. Sci. Eng.: A 872 (2023) 145001, http://dx.doi.org/10.1016/j.msea.2023.145001.

[42] C. Lauff, M. Schneider, J. Montesano, T. Böhlke, Generating microstructures of long fiber reinforced composites by the fused sequential addition and migration method, Internat. J. Numer. Methods Engrg. 125 (2024) e7573, http://dx.doi.org/10.1002/NME.7573.

[43] C. Lauff, M. Krause, M. Schneider, .T. Böhlke, On the influence of the fiber curvature on the stiffness of long fiber reinforced composites, Internat. J. Numer. Methods Engrg. 126 (2025) e70094, http://dx.doi.org/10.1002/NME.70094.

[44] S. Gajek, M. Schneider, T. Böhlke, An FE-DMN method for the multiscale analysis of short fiber reinforced plastic components, Comput. Methods Appl. Mech. Engrg. 384 (2021) 113952, http://dx.doi.org/10.1016/J.CMA.2021.113952.

[45] S. Forest, Micromorphic Media, in: H. Altenbach, V.A. Eremeyev (Eds.), Generalized Continua from the Theory To Engineering Applications, Springer, Vienna, 2013, pp. 249–300, http://dx.doi.org/10.1007/978-3-7091-1371-4_5.

[46] Z. Yang, Y. Sun, Y. Liu, Q. Ma, A second-order multiscale approach for viscoelastic analysis of statistically inhomogeneous materials, Compos. Struct. 220 (2019) 550–565, http://dx.doi.org/10.1016/j.compstruct.2019.04.044.

[47] F.L. Palombini, W. Kindlein, B.F. De Oliveira, J.E. De Araujo Mariath, Bionics and design: 3D microstructural characterization and numerical analysis of bamboo based on X-ray microtomography, Mater. Charact. 120 (2016) 357–368, http://dx.doi.org/10.1016/j.matchar.2016.09.022.

[48] J. Cui, Z. Qin, A. Masic, M.J. Buehler, Multiscale structural insights of load bearing bamboo: A computational modeling approach, J. Mech. Behav. Biomed. Mater. 107 (2020) 103743, http://dx.doi.org/10.1016/j.jmbbm.2020.103743.

[49] L.S. Al-Rukaibawi, S.L. Omairey, G. Károlyi, A numerical anatomy-based modelling of bamboo microstructure, Constr. Build. Mater. 308 (2021) 125036, http://dx.doi.org/10.1016/j.conbuildmat.2021.125036.

[50] M. Khajouei-Nezhad, M. Mokarizadehhaghighishirazi, V. Nasir, S.V. Lomov, B. Buffel, F. Desplentere, C. Dai, Elastic behaviour of bamboo at nano- and microscale, Constr. Build. Mater. 431 (2024) 136579, http://dx.doi.org/10.1016/J.CONBUILDMAT.2024.136579.

[51] M.E. Gurtin, E. Fried, L. Anand, The Mechanics and Thermodynamics of Continua, Cambridge University Press, 2010.

[52] M. Moakher, Fourth-order cartesian tensors: old and new facts, notions and applications, Quart. J. Mech. Appl. Math. 61 (2) (2008) 181–203, http://dx.doi.org/10.1093/qjmam/hbm027.

[53] J. Ohser, F. Mücklich, Statistical Analysis of Microstructures in Materials Science, John Wiley & Sons, 2000, pp. 25–30.

[54] T. Böhlke, K. Jöchen, R. Piat, T.A. Langhoff, I. Tsukrov, B. Reznik, Elastic properties of pyrolytic carbon with axisymmetric textures, Tech. Mech. - Eur. J. Eng. Mech. 30 (2010) 343–353.

[55] S.G. Advani, C.L. Tucker, The use of tensors to describe and predict fiber orientation in short fiber composites, J. Rheol. 31 (1987) 751–784, http://dx.doi.org/10.1122/1.549945.

[56] I. Arganda-Carreras, V. Kaynig, C. Rueden, K.W. Eliceiri, J. Schindelin, A. Cardona, H. Sebastian Seung, Trainable weka segmentation: a machine learning tool for microscopy pixel classification, Bioinform. 33 (15) (2017) 2424–2426, http://dx.doi.org/10.1093/bioinformatics/btx180.

[57] J. Schindelin, I. Arganda-Carreras, E. Frise, V. Kaynig, M. Longair, T. Pietzsch, S. Preibisch, C. Rueden, S. Saalfeld, B. Schmid, J.Y. Tinevez, D.J. White, V. Hartenstein, K. Eliceiri, P. Tomancak, A. Cardona, Fiji: an open-source platform for biological-image analysis, Nat. Methods 9 (2012) 676–682, http://dx.doi.org/10.1038/nmeth.2019, 2012 9:7.

[58] G. Jocher, J. Qiu, A. Chaurasia, Ultralytics YOLO, 2023, URL https://github.com/ultralytics/ultralytics.

[59] H. Imai, M. Iri, K. Murota, VORONOI diagram in the LAGUERRE geometry and its applications., SIAM J. Comput. 14 (1985) 93–105, http://dx.doi.org/10.1137/0214006.

[60] M. Schneider, The sequential addition and migration method to generate representative volume elements for the homogenization of short fiber reinforced plastics, Comput. Mech. 59 (2017) 247–263, http://dx.doi.org/10.1007/S00466-016-1350-7.

[61] A.G. Fokin, Solution of statistical problems in elasticity theory in the singular approximation, J. Appl. Mech. Tech. Phys. 13 (1972) 85–89, http://dx.doi.org/10.1007/BF00852360/METRICS.

[62] J.D. Eshelby, The determination of the elastic field of an ellipsoidal inclusion, and related problems, Proc. R. Soc. Lond. Ser. A. Math. Phys. Sci. 241 (1226) (1957) 376–396.

[63] J.R. Willis, Bounds and self-consistent estimates for the overall properties of anisotropic composites, J. Mech. Phys. Solids 25 (1977) 185–202, http://dx.doi.org/10.1016/0022-5096(77)90022-9.

[64] L.J. Walpole, On bounds for the overall elastic moduli of inhomogeneous systems—I, J. Mech. Phys. Solids 14 (1966) 151–162, http://dx.doi.org/10.1016/0022-5096(66)90035-4.

[65] A. Morawiec, Orientations and Rotations, Springer Berlin Heidelberg, 2004, http://dx.doi.org/10.1007/978-3-662-09156-2.

[66] A. Reuss, Berechnung der Fliessgrenze von Mischkristallen auf Grund der Plastizitätsbedingung für Einkristalle., ZAMM - J. Appl. Math. Mech. / Z. Angew. Math. Mech. 9 (1) (1929) 49–58, http://dx.doi.org/10.1002/zamm.19290090104.

[67] W. Voigt, Ueber die Beziehung zwischen den beiden Elasticitätsconstanten isotroper Körper, Ann. Phys., Lpz. 274 (12) (1889) 573–587.

[68] M. Lobos, T. Böhlke, On optimal zeroth-order bounds of linear elastic properties of multiphase materials and application in materials design, Int. J. Solids Struct. 84 (2016) 40–48, http://dx.doi.org/10.1016/J.IJSOLSTR.2015.12.015.

[69] E. Kröner, Bounds for effective elastic moduli of disordered materials, J. Mech. Phys. Solids (1977) 137–155, http://dx.doi.org/10.1016/0022-5096(77)90009-6.

[70] H. Moulinec, P. Suquet, A numerical method for computing the overall response of nonlinear composites with complex microstructure, Comput. Methods Appl. Mech. Engrg. 157 (1) (1998) 69–94, http://dx.doi.org/10.1016/S0045-7825(97)00218-1.

[71] M. Schneider, F. Ospald, M. Kabel, Computational homogenization of elasticity on a staggered grid, Internat. J. Numer. Methods Engrg. 105 (9) (2016) 693–720, http://dx.doi.org/10.1002/nme.5008.

[72] J. Zeman, J. Vondřejc, J. Novák, I. Marek, Accelerating a FFT-based solver for numerical homogenization of periodic media by conjugate gradients, J. Comput. Phys. 229 (2010) 8065–8071, http://dx.doi.org/10.1016/J.JCP.2010.07.010.

[73] T. Böhlke, C. Brüggemann, Graphical representation of the generalized Hooke's law, Tech. Mech. 21 (2) (2001) 145–158.

[74] Y. Akinbade, K.A. Harries, C.V. Flower, I. Nettleship, C. Papadopoulos, S. Platt, Through-culm wall mechanical behaviour of bamboo, Constr. Build. Mater. 216 (2019) 485–495, http://dx.doi.org/10.1016/j.conbuildmat.2019.04.214.

[75] R. Moran, K. Webb, K. Harries, J.J. García, Edge bearing tests to assess the influence of radial gradation on the transverse behavior of bamboo, Constr. Build. Mater. 131 (2017) 574–584, http://dx.doi.org/10.1016/j.conbuildmat.2016.11.106.

[76] B. Sharma, K.A. Harries, K. Ghavami, Methods of determining transverse mechanical properties of full-culm bamboo, Constr. Build. Mater. 38 (2013) 627–637, http://dx.doi.org/10.1016/j.conbuildmat.2012.07.116.

[77] B. Shu, L. Hong, S. Li, Y. Tao, J. Cui, N. Fu, J. Yu, C. Li, X. Lu, Study on the Tangential Tensile Mechanical Properties of Moso Bamboo, J. Renew. Mater. 10 (8) (2022) 2203–2216, http://dx.doi.org/10.32604/jrm.2022.019882.

[78] X. Li, W. Wang, L. Wu, S. Chen, X. Hu, J. Li, J. Tang, J. Yang, Generalized Focal Loss: Learning Qualified and Distributed Bounding Boxes for Dense Object Detection, 2020, http://dx.doi.org/10.48550/arXiv.2006.04388, arXiv:2006.04388 [cs].

[79] L.J. Walpole, On the overall elastic moduli of composite materials, J. Mech. Phys. Solids 17 (4) (1969) 235–251, http://dx.doi.org/10.1016/0022-5096(69)90014-3.

[80] T. Kanit, S. Forest, I. Galliet, V. Mounoury, D. Jeulin, Determination of the size of the representative volume element for random composites: statistical and numerical approach, Int. J. Solids Struct. 40 (2003) 3647–3679, http://dx.doi.org/10.1016/S0020-7683(03)00143-4.

[81] R. Hill, Elastic properties of reinforced solids: Some theoretical principles, J. Mech. Phys. Solids 11 (1963) 357–372, http://dx.doi.org/10.1016/0022-5096(63)90036-X.

[82] W.J. Drugan, J.R. Willis, A micromechanics-based nonlocal constitutive equation and estimates of representative volume element size for elastic composites, J. Mech. Phys. Solids 44 (1996) 497–524, http://dx.doi.org/10.1016/0022-5096(96)00007-5.

[83] A. Gloria, F. Otto, An optimal variance estimate in stochastic homogenization of discrete elliptic equations, 39, (ISSN: 0091-1798) 2011, pp. 779–856, http://dx.doi.org/10.1214/10-AOP571.

[84] L. Speichinger, R. Förster, T. Böhlke, Dataset for vascular bundle detection in moso bamboo, 2026, http://dx.doi.org/10.35097/fe5eamg8w89bx4ns.

[85] L. Speichinger, R. Förster, T. Böhlke, Cross-sectional images of moso bamboo mesostructure, 2026, http://dx.doi.org/10.35097/j5ut6hq62v0506ye.